5. Defects in Monocrystalline Silicon

Wilfried von Ammon, Andreas Sattler, Gudrun Kissinger

The aggregation of instrinsic point defects (vacancies and Si interstitials) in monocrystalline silicon has a major impact on the functioning of electronic devices. While agglomeration of vacancies results in the formation of tiny holes (so-called *voids*, around 100 nm in size, which have almost no stress field), the aggregation of Si interstitials exerts considerable stress on the Si matrix, which, beyond a critical size, generates a network of dislocation loops around the original defect. These dislocation loops are typically microns in size. Consequently, they are much more harmful to device functioning than vacancy clusters. However, the feature size in electronic devices has now shrunk below the 100 nm scale, meaning that vacancy aggregates are also no longer acceptable to many device manufacturers.

This chapter is intended to give an introduction to the properties of intrinsic point defects in silicon and the nucleation and growth of their aggregates. Knowledge in this field has grown further over the last decade. It is now possible to accurately simulate the aggregation process so that the defect behavior of semiconductor silicon can be precisely tailored to the needs of the device manufacturer. Additionally, the impact of various impurities on the aggregation process is elucidated.

5.1 **Technological Impact of Intrinsic Point Defects Aggregates** 112
5.2 **Thermophysical Properties of Intrinsic Point Defects** 113
5.3 **Aggregates of Intrinsic Point Defects** 115
5.3.1 Experimental Observations 115
5.3.2 Theoretical Model: Incorporation of Intrinsic Point Defects 118
5.3.3 Theoretical Model: Aggregation of Intrinsic Point Defects 120
5.3.4 Effect of Impurities on Intrinsic Point Defect Aggregation 123
5.4 **Formation of OSF Ring** 127
References 129

As the feature size continues to shrink in device industry and now approaches a design rule of 7 nm, a thorough understanding of defect behavior in bulk silicon is of utmost importance. Three major defect types relevant to device performance have been identified:

1. Vacancy aggregates (known as *voids*, which usually have a size of less than 150 nm)
2. Si interstitial clusters embedded in a network of dislocation loops, each of which extend over several microns (L-pits)
3. Large grown-in oxygen precipitates.

The latter generate stacking faults (OSF) during wafer oxidation. The voids form in the center of the crystal, while L-pits are observed in the outer region. The two concentric defect regions are usually separated by a small OSF ring. The type of defect that develops in the growing crystal is determined by a simple parameter: the ratio of the pull rate to the temperature gradient at the growth interface. In industry, crystals with only one type of defect – voids – are produced almost exclusively. The formation and behavior of voids has been studied intensively and is accurately described by current theoretical models. As the feature size is now smaller than the void size in standard silicon crystals, the growth of so-called *perfect silicon* with almost no detectable defects may be adopted. Furthermore, the doping of crystals with impurities like nitrogen or carbon is being widely investigated. These impurities can significantly reduce the defect size, but they may also have harmful effects, such as enhancing the generation of OSFs. Some models have recently been proposed which may allow us to predict some of the effects of impurities.

© Springer International Publishing AG 2017
S. Kasap, P. Capper (Eds.), *Springer Handbook of Electronic and Photonic Materials*, DOI 10.1007/978-3-319-48933-9_5

5.1 Technological Impact of Intrinsic Point Defects Aggregates

Single intrinsic point defects in silicon – vacancies and interstitials – have not been found to have any negative impact on device performance so far. However, if they aggregate into clusters they can be even detrimental to device functionality. This is also true of extended defects like dislocations. When silicon wafer technology was in its formative years, much of the work devoted to improve wafer quality focused on controlling dislocation density in the silicon crystals, as it was not possible to grow dislocation-free crystals. However, with the introduction of dislocation-free crystal growth processes into mass production, the issue of extended dislocations in relation to bulk silicon quality vanished. As the feature size decreased and the demand for higher device performance increased, it soon became apparent that intrinsic point defects and their aggregation during the cool-down phase of the crystal growth process were having an increasingly negative impact on device performance and yield. Historically, one of the first serious challenges in this regard was the aggregation of Si interstitials in floating zone (FZ)-grown crystals, which results in a local network of dislocation loops (secondary defects), so-called *A-swirls* [5.1] or L-pits [5.2]. Although the diameters of these dislocation loops are only a few microns, they are large enough to generate hot spots in the space charge regions of high-power devices [5.3, 4]. In the second half of the 1980s, the industry began to encounter problems with the early breakdown of the gate oxide in memory devices based on Czochralski (CZ)-grown silicon [5.5]. After intensive gate oxide integrity (GOI) investigations, it was found that the root cause of the gate oxide degradation was tiny micro holes – voids – which were formed by vacancy aggregation during crystal growth [5.6, 7]. Each void is thermally stabilized by an oxide layer present on its inner surface. After wafer polishing, the voids show up as dimples or laser light scattering (LLS) defects on the wafer surface, causing a local thinning of the gate oxide [5.8, 9]. Voids are considerably smaller (less than 150 nm) than A-swirl defects, and so their impact on device performance is only apparent if the location of a void coincides with that of an active element, such as a transistor. In addition, most of these defective transistors can be repaired due to the built-in redundancy of memory chips. Consequently, vacancy aggregates are tolerable for many devices, so long as their density is insignificant compared to those of device process-induced defects. This should be contrasted with A-swirls or L-pits, which always result in permanent device damage due to their large sizes.

Empirically, it has been found that gate oxides 40−50 nm thick are most susceptible to void defects [5.9]. Thinner oxides show higher GOI yields, and when the thickness drops below 5 nm the influence of voids on the GOI yield disappears [5.10, 11]. However, as the feature size continues to shrink, additional adverse effects have been identified, such as shorts between trench capacitors and lack of device reliability [5.12, 13]. As the design rule becomes equal to or less than the void size, these problems are expected to aggravate and device manufacturers may have to switch to materials with extremely small defect sizes or those that contain virtually no defects.

There are three main ways to achieve silicon with no harmful intrinsic point defect aggregates. The first is to grow silicon crystals in a regime where Si interstitials and vacancies are incorporated in equal concentrations (Sect. 5.3.2), resulting in almost complete mutual annihilation of point defects (so-called *perfect* or *pure* silicon) [5.14–17]. The method inevitably involves lower pull rates and very tight control over crystal growth parameters, which yields considerably lower throughput and higher costs, in particular for 300 mm crystal growth.

The second approach is the growth of nitrogen-doped crystals with very fast pull rates (high cooling rates) and subsequent high-temperature (≈1200 °C) wafer annealing [5.18]. Nitrogen doping in conjunction with a fast pull rate decreases the vacancy aggregate size (Sect. 5.3.3 and Sect. 5.3.4) [5.18, 19], meaning that they are easy to dissolve using a high-temperature wafer treatment. Void annihilation first requires the dissolution of the inner oxide layer, which in turn, necessitates the outdiffusion of oxygen. Thus, annealed wafers only exhibit a near-surface defect-free region ≈10 μm in depth, which is, however, sufficient for device manufacturing. Annealed wafers also take advantage of the notable mechanical strengthening effects of nitrogen doping [5.20–22], which helps to suppress slippage generation during high-temperature treatment. One very recent development is rapid thermal wafer annealing at a temperature of around 1300 °C. At this temperature, outdiffusion of oxygen is not necessary because the oxygen concentration is usually below that required for oxygen solubility, so the inner oxide layer dissolves throughout the bulk and the voids collapse. This process yields silicon of a similar quality to that resulting from perfect silicon crystal growth.

The third method is the well-known epi wafer approach.

All of these methods require rather precise defect engineering in order to obtain the properties demanded by the device industry, except in the case of pp + epi wafers. Here, the high boron concentration of the substrate suppresses intrinsic point defect aggregation (Sect. 5.3.4) and enhances oxygen precipitation in the bulk. Therefore, this wafer type not only provides a defect-free epi layer, but also provides high slip resistances and superior internal gettering (impurity removal) abilities of metallic contaminants.

5.2 Thermophysical Properties of Intrinsic Point Defects

Understanding intrinsic point defect aggregation undoubtedly requires rather exact knowledge of their respective thermophysical properties.

The intrinsic point defects – vacancies and Si interstitials – can exist in different configurations. Generally, six localized point defect configurations of high symmetry are considered: the vacancy and the split-vacancy on the one hand, and the tetrahedral, the hexagonal, the bond-centered and the [100] split or dumbbell Si interstitial on the other [5.23]. While the localized configuration works rather well for vacancies, theoretical calculations strongly favor an extended configuration of lower symmetry for Si interstitials [5.24, 25]. The extended self-interstitial model was originally proposed to explain the high pre-exponential factor in the coefficient of self-diffusion, and this model now has support from theoretical calculations [5.23, 26, 27]. According to theory, the high value of the pre-exponential factor results from the multitude of self-interstitial configurations with similar energies and the significant lattice relaxations that accompany some of these configurations.

Vacancies and Si interstitials can also exist in various charged states (such as $V^{2+}, V^{+}, V^{0}, V^{-}, V^{2-}$), and at the high temperatures ($> 1000\,°C$) where point defects start to aggregate all states should be present in dynamic equilibrium [5.28]. Due to this equilibration, it is not meaningful to assign a specific charge to vacancies and Si-interstitials, respectively. However, atomistic calculations show that the charged states are much higher in energy and so their populations should be negligible. So far, there is no indication that charged states have any impact on defect aggregation and so they are not considered in current defect nucleation models.

Unfortunately, it is generally not possible to observe intrinsic point defects directly and, consequently, their thermophysical properties cannot be measured directly either. Thus, indirect approaches must be used that involve fitting defect concentrations along with many other parameters. Various experimental systems have been used to infer the thermophysical properties of point defects. The most common of these are metal diffusion experiments where a metallic contaminant such as zinc, gold or platinum is introduced into the bulk via high-temperature drive-in diffusion [5.29–31]. The diffusion rate of the metallic impurity, which is easily detectable using standard methods, is related to the mobility and the concentration of intrinsic point defects (kick-out and Frank–Turnbull mechanism), which provides a way to indirectly probe the behavior of the point defects. These experiments yield good estimates for the product $C_{eq}D$ of the equilibrium concentration C_{eq} and the diffusivity D for self-interstitials I and vacancies V, respectively. The following values are derived from zinc diffusion results [5.32]

$$C_{I}^{eq}D_{I} = 1.5\times10^{26}\exp\left(\frac{-4.95\,\text{eV}}{k_{B}T}\right)\text{cm}^{-1}\,\text{s}^{-1}$$

and

$$C_{V}^{eq}D_{V} = 1.3\times10^{23}\exp\left(\frac{-4.24\,\text{eV}}{k_{B}T}\right)\text{cm}^{-1}\,\text{s}^{-1}\,.$$

Another frequently used experimental method is the defect analysis of CZ crystals grown with varying pull rates. In this case, the observables are the dynamic responses of the oxidation-induced stacking fault (OSF) ring and the interstitial–vacancy boundary as a function of changes in crystal growth process conditions [5.2, 33–35] (Sect. 5.4). These observables have been quantitatively correlated to intrinsic point defect distributions in crystals and, therefore, can be used to derive thermophysical properties [5.36]. Of particular importance is the complementary nature of crystal growth and metal diffusion experiments with regard to parametric sensitivity. Its sensitivity to self-interstitial and vacancy competition implies that these experiments are suitable for determining some pre-exponential coefficients. The metal diffusion experiments, which can be carried out over a wide range of temperatures, are particularly useful for probing activation energies.

Rapid thermal annealing (RTA) experiments with fast cooling rates have been carried out with silicon wafers to investigate the influence of the free vacancy concentration on oxygen precipitation [5.17, 37]. By heating the wafers to above $1150\,°C$, detectable concentrations of Frenkel pairs are created in the wafer bulk. The wafer is then held at this temperature for around 10 s to allow the self-interstitials to diffuse

out, resulting in a near-equilibration of both interstitials $[C_I^{eq}(T)]$ and vacancies $[C_V^{eq}(T)]$. Following this rapid equilibration, the wafer is rapidly cooled (at rates of $\approx 100\,°C/s$) to freeze in the vacancy excess which can subsequently be probed via its impact on oxygen precipitation. This technique is especially useful for gaining information on $[C_V^{eq}(T) - C_I^{eq}(T)]$ at various temperatures [5.38]. Quenching experiments at different holding temperatures are also reported for hydrogen-doped samples, which allow us to quantitatively measure the VH_4 complex [5.39]. From these results, the vacancy formation energy was deduced as $\approx 4\,eV$ with relatively good accuracy.

Experimental data that relate to the recombination coefficient of vacancies and Si interstitials are scarce [5.40, 41]. Nevertheless, there is general agreement that recombination between vacancies and Si interstitials is so fast that the product of the concentrations of both species is always in thermal equilibrium. The exact value is therefore not relevant to subsequent discussion here.

There have been numerous attempts to compute the thermophysical properties of point defects directly by atomistic simulations. The most important aspect of these atomistic calculations is the accuracy of the assumed interatomic interaction. As the ab initio approach, which explicitly considers electronic interactions, is extremely computationally expensive and therefore limited to small systems and zero temperature, most simulations are carried out using empirical potentials, such as the Stillinger–Weber or Tersoff potential functions, discarding explicit representations of electronic interactions. An excellent overview of this field is given by *Sinno* [5.42]. A parameter set that yields rather good results for defect aggregation is shown in Fig. 5.1. It is clear that the difference between the vacancy and Si interstitial concentrations at the melting point is only around 30% in favor of vacancies. On the other hand, vacancies diffuse more slowly than Si interstitials. These two properties are of great relevance to the peculiar defect behavior of silicon.

In the past, fitted values for equilibrium concentrations and diffusivities inferred from various experimental data often spread over many orders of magnitude, meaning that they were of little help. However, in recent years, theoretical methods and the accuracy of experimental data have significantly improved and the predicted values are now in much better agreement with those gleaned from experiments.

Recently, another impact factor became obvious which may have led to different fit results of the thermophysical data of the past. As described in detail later in Sect. 5.3.2, the solubility of the intrinsic point defects is obviously dependent on the thermal stress which is

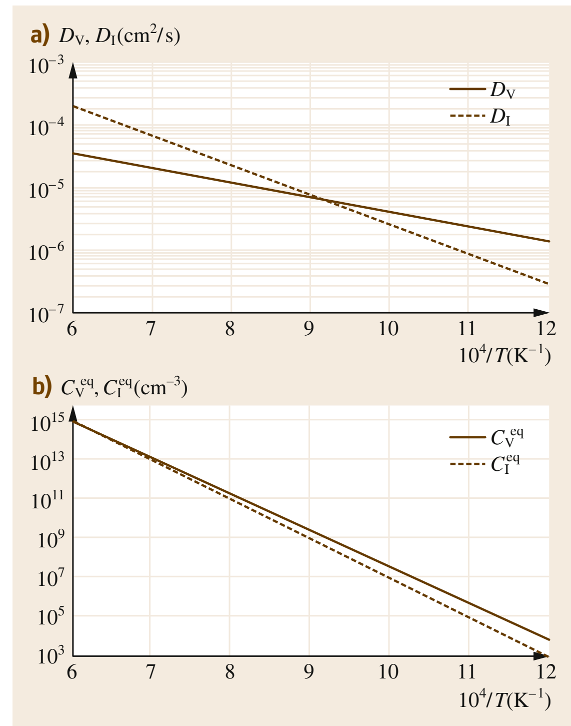

Fig. 5.1a,b Diffusivities and equilibrium concentrations of vacancies and Si interstitials, respectively. (After [5.43])

imposed on the crystal during growth [5.44]. In addition, the diffusivities of the intrinsic point defects are believed to be affected by stress, too. *Sueoka* et al. used density functional theory (DFT) calculations to determine the stress dependence of the formation enthalpies of vacancies and interstitials [5.45]. The best agreement between experimental and simulated values was obtained for plane thermal stress. Sueoka's ab initio calculations lead to the following dependencies of the formation enthalpies of vacancies (H_f^V) and interstitials (H_f^I) on the average plane stress (σ_{ave})

$$H_f^V\,(eV) = 0.308 \times \sigma_{ave}$$

and

$$H_f^I\,(eV) = -0.069 \times \sigma_{ave}$$

with σ_{ave} given in GPa. The relationship is valid in the range $-1\,GPa < \sigma_{ave} < 0\,GPa$, and the average plane stress is defined as $\sigma_{ave} = (\sigma_X + \sigma_Y)/3$. The effect of stress on the formation energies seems small, but these small differences have a notable influence on ξ_{tr} (see (5.1) in Sect. 5.3.2), the parameter which determines the incorporation of the predominant defect type in a growing crystal.

In another work, *Sueoka* et al. [5.46] used DFT calculations to obtain the formation energies of vacancies and interstitials at all sites within a sphere around a dopant atom in silicon [5.46]. This was done for substitutional p-type (B and Ga), neutral (C, Ge, and Sn), and n-type (P, As, Sb, and Bi) dopants. In this way, thermal equilibrium concentrations of vacancies and interstitials were obtained for various dopants and doping levels. For details see [5.46].

5.3 Aggregates of Intrinsic Point Defects

5.3.1 Experimental Observations

As pointed out in Sect. 5.1, the dominant intrinsic point defect aggregates in silicon single crystals are voids and L-pits/A-swirls. Figure 5.2 shows a transmission electron microscope (TEM) image of a void with a 5 nm oxide layer on the inner surface. Oxidation of the inner surface is not observed in FZ crystals due to their very low oxygen contents. The thickness of the oxide layer decreases with increasing cooling rate of the growing crystal. A strain field is generally not observed around the void. Usually, voids exhibit octahedral morphologies, but they can change to platelet or even rodlike shapes if the crystal is doped with nitrogen (Sect. 5.3.4). Under standard growth conditions, twin voids consisting of two partial octahedral voids are predominantly observed [5.47, 48]. At lower oxygen contents and higher cooling rates of the growing crystals, single octahedral voids are preferentially formed [5.49, 50]. Typical sizes range from 70–200 nm depending on the crystal growth conditions. Historically, different notations were introduced for this type of defect depending on their delineation or the detection technique used:

- Crystal originated particle (COP) [5.51]
- Laser light scattering tomography defect (LSTD) [5.2]
- Flow pattern defect (FPD) [5.52]
- D-defects [5.53].

Today, it is generally accepted that they all denote the same defect type: vacancy aggregates.

The TEM image of an L-pit is depicted in Fig. 5.3. The network of perfect dislocation loops characteristic of this defect type is clearly visible. The core of the defect is a self-interstitial aggregate which forms an extrinsic stacking fault [5.55, 56]. When the stacking fault reaches a critical size, the strain exerted on the crystal lattice is relaxed by the generation of dislocation loops. It is believed that the B-swirl observed in FZ crystals [5.57, 58] is most likely related to self-interstitial aggregates with sizes below the critical limit [5.59, 60]. While the B-swirl can be annihilated by appropriate high-temperature treatment, the L-pit/A-swirl is extremely stable.

In the case of epi wafers, voids at the substrate surface are covered by the epilayer and no defects are generated in the epilayer. However, if the layer thickness is very thin ($< 1\,\mu m$), a dimple remains at the epi-

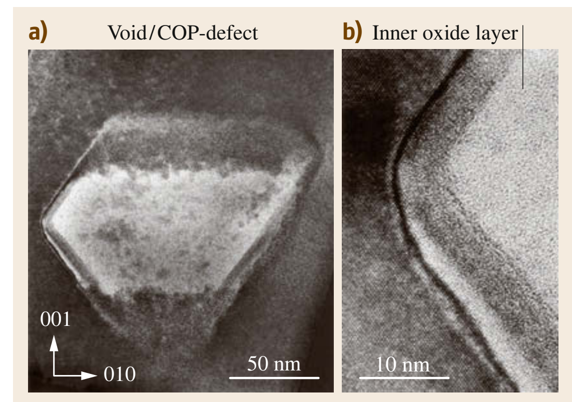

Fig. 5.2a,b TEM picture of a void/COP **(a)**. The inner surface of the void is cover by an oxide layer **(b)**. (After [5.54])

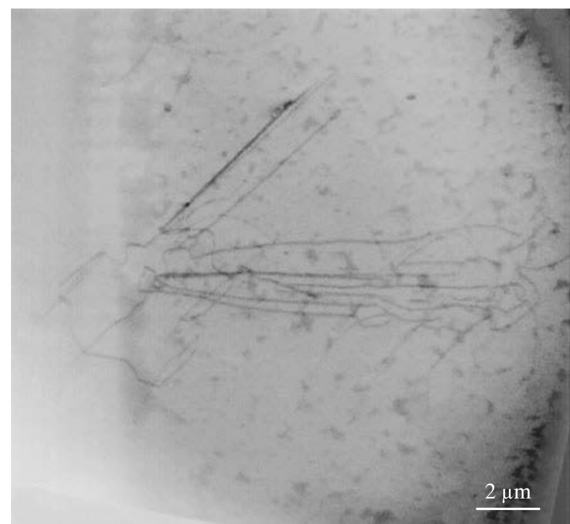

Fig. 5.3 TEM picture of an L-pit. (After [5.55])

layer surface which is detectable by laser light scattering [5.61]. In contrast to voids, L-pits always generate clearly visible and harmful defects in the epilayer [5.62] and are therefore unacceptable to device manufacturers. It is well-established that the pull rate V and the axial temperature gradient G at the growth interface of the growing crystal have the biggest influence on the defect types that develop in the growing crystal [5.33, 34, 63] and their spatial [5.35] as well as their density/size distributions [5.64]. At high pull rates, vacancy-related defects (voids) are observed over the entire crystal volume (Fig. 5.4). When the pull rate is reduced, oxidation-induced stacking faults (OSFs) develop in a small ring-like region near the crystal rim [5.65]. If the pull rate is decreased further, the ring diameter shrinks and L-pits are detected in the area outside the OSF ring [5.2]. No voids are found in this outer region. Thus, the OSF ring obviously represents the spatial boundary between vacancy- and self-interstitial-type defects. At a critical pull rate, the void region and the OSF ring disappear completely and only L-pits are detected. In FZ crystals with their inherently low oxygen contents, no OSF ring is observed as a boundary; instead a defect free-zone is observed as the boundary [5.66].

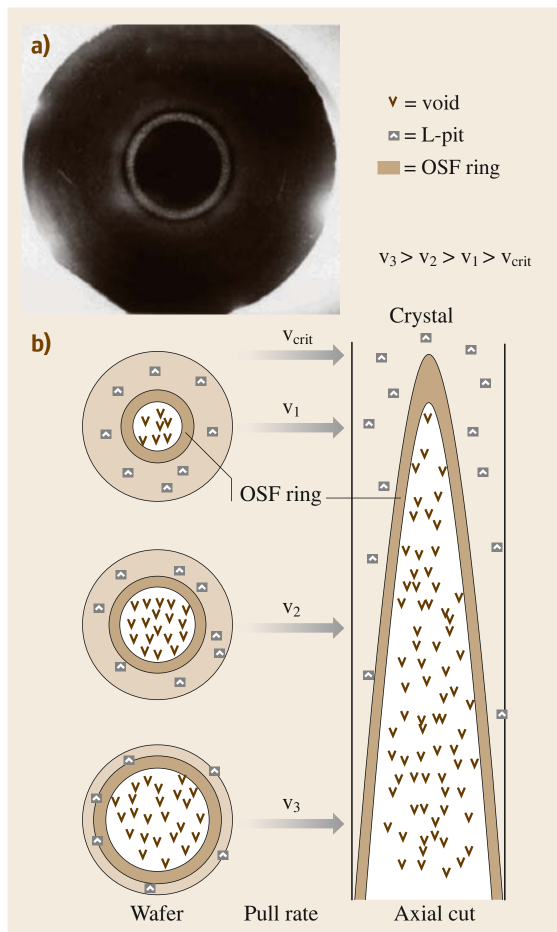

Fig. 5.4a,b Variation in the radial defect behavior of a CZ crystal as a function of pull rate. **(b)** shows a wafer from the crystal part grown with medium pull rate. The defects were delineated by Secco etching

The radial position of the OSF ring can be approximately described by the equation [5.35]

$$\frac{V}{G(r)} = \xi_{tr} = 1.34\times10^{-3}\,\mathrm{cm^2\,K^{-1}\,min^{-1}}\,.$$

Here r is the radial position. Recently, somewhat higher values for ξ_{tr} are proposed [5.44]. Thus, the parameter V/G controls the type of grown-in defect: if $V/G > \xi_{tr}$ vacancy aggregates develop, while for $V/G < \xi_{tr}$ Si interstitial-related defects are observed. This was first recognized by *Voronkov* in 1982 [5.63], who derived the following relation between ξ_{tr} and the thermophysical properties of intrinsic point defects

$$\xi_{tr} = \frac{(\Delta H_I + \Delta H_V)\left(D_I C_I^{eq}(T_0) - D_V C_V^{eq}(T_0)\right)}{2k_b T_0^2\left(C_V^{eq}(T_0) - C_I^{eq}(T_0)\right)}\,. \tag{5.1}$$

A further important parameter for the control of grown-in defects is the thermal history of the crystal. While its influence on the type of defect that develops in the growing crystal is negligible, detailed investigations have revealed a strong effect of cooling rate on the defect density/size distribution. For a crystal cooling in the temperature range between roughly 1000 and 1100 °C, there seems to be an exponential relation between the void density N_{void} and the dwell time t (Fig. 5.5) [5.67]. The defect density data in Fig. 5.5 were derived from GOI measurements that can detect much smaller defect sizes than delineation techniques based on etching and/or laser light scattering. The correlation between the various detection methods down to sizes of 0.12 µm was found to be rather good [5.18]. The exact upper value of the above temperature range depends on the crystal growth conditions and will be shown (Sect. 5.3.3) to coincide with the void nucleation temperature. The width of the selected temperature interval, on the other hand, does not have much impact on the above empirical relation. As will be discussed below, the relevant temperature interval is rather small [5.68]. Hence, the dwell time might just as well be replaced by the inverse of the cooling rate at the nucleation temperature.

It was further observed that the average void size increases as dwell time increases (with slower cooling rates) and vice versa (Fig. 5.6) [5.64, 69]. Another

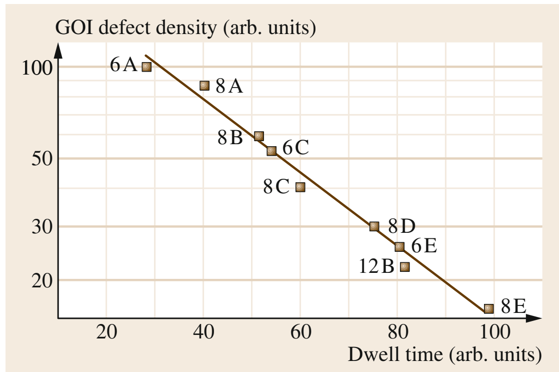

Fig. 5.5 Void density as derived from GOI measurements as a function of the dwell time of the growing crystal at ≈1100 °C. The *straight line* denotes simulation results. The various data points relate to different growth processes. (After [5.64])

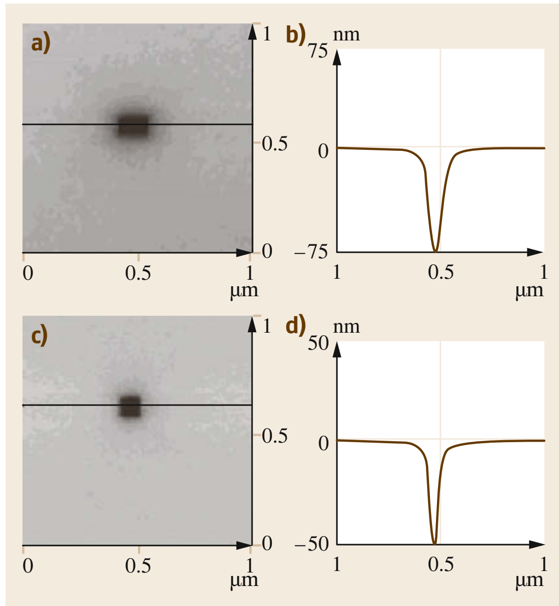

Fig. 5.6a–d Atomic force microscopy measurements of voids at the wafer surface **(a,c)** and their respective depth profiles **(b,d)**. The depth of the surface void is rather close to its original size in the crystal. **(a)** and **(b)** refer to a slowly cooled and **(c)** and **(d)** to a rapidly cooled crystal. (After [5.61])

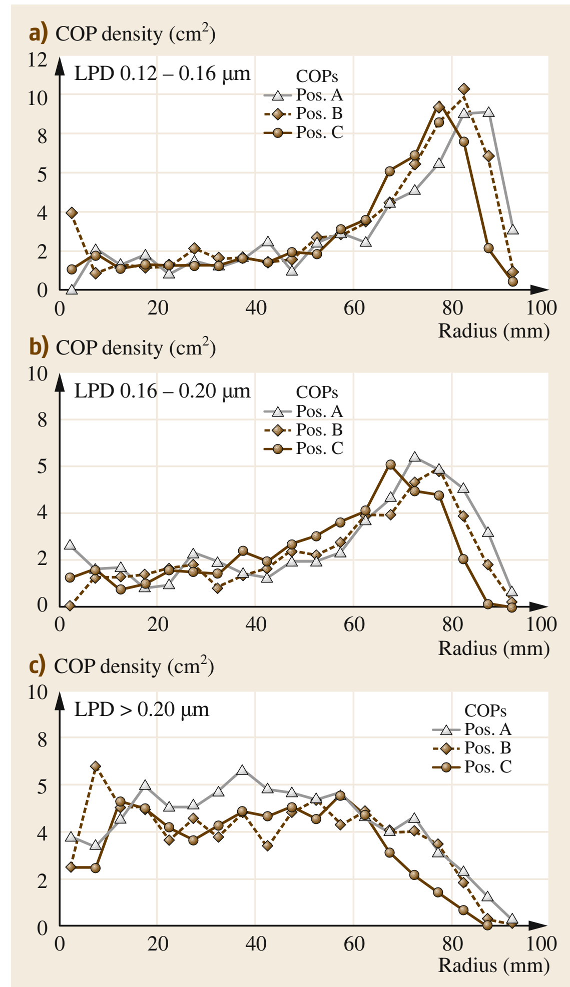

Fig. 5.7a–c Radial variation in the density/size distribution of voids/COPs across a wafer as measured by laser light scattering. The light point defect size (LPD) correlates well to the actual void size. The positions *A*, *B* and *C* relate to different axial crystal positions

striking feature is the characteristic change in the defect density/size distribution across the crystal diameter (Fig. 5.7) [5.70]. While large voids of low density prevail in the crystal center, the distribution gradually shifts to small sizes and high density towards the boundary of the void region. As the cooling rates of the crystal center and rim are almost the same, this remarkable variation in the density/size distribution must be related to the radial inhomogeneity of $V/G(r)$. Unfortunately, similar data are not yet available for L-pits. The behavior of this defect type is more complex, as small interstitial aggregates which do not generate dislocation loops are not detected as L-pits.

Valuable information about the defect nucleation temperature is obtained from transient growth experiments where the pull rate is reduced to zero and the growth process is halted when a certain crystal length has been reached [5.71–73]. After a certain amount of time has elapsed, growth is resumed and the crystal is grown to full length. During the halting period, the various crystal positions are at different temperatures ac-

cording to the axial temperature gradient of the crystal. By analyzing the axial defect behavior of the as-grown crystal, one can identify the temperature ranges where specific defect types nucleate and grow in size. The results of those experiments clearly demonstrated that the nucleation temperature of voids lies between 1000 and 1100 °C and varies with the growth conditions. It was also demonstrated that the nucleation and growth period of the voids occurs over a temperature interval of less than 50 K [5.74]. Void growth is then obviously stopped by the formation of the inner oxide layer. The oxide layer continues to grow down to relatively low temperatures. The scarce data available for L-pits indicate a similar temperature range for nucleation [5.75].

5.3.2 Theoretical Model: Incorporation of Intrinsic Point Defects

The incorporation of intrinsic point defects is the result of two competing fluxes at the growth interface: a vacancy and an interstitial flux which are both directed into the crystal (Fig. 5.8). Each of the two fluxes consists of two components. The first flux component is driven by the advancing growth interface, which generates a convective flux proportional to the pull rate V, and the second is driven by the vacancy/interstitial recombination behind the interface, which creates a concentration gradient and, in turn, a Fickian diffusion flux. The latter is proportional to G. If the pull rate is low, then the Fickian diffusion dominates over the convective flux. As self-interstitials diffuse significantly faster than vacancies, the self-interstitial flux wins over the vacancy flux. During crystal cooling, V–I recombination virtually eliminates the vacancies and the surviving self-interstitials are driven into supersaturation and finally aggregate. On the other hand, at fast pull rates the convective flux dominates and, due to the larger equilibrium concentration of vacancies compared to that of self-interstitials, more vacancies flow into the crystal, resulting in vacancy aggregates. A similar change in the prevailing defect type is obtained when G is varied. The above model, originally proposed by *Voronkov* [5.63], yields the previously mentioned parameter V/G which determines the defect type.

In standard growth processes, G always exhibits a notable increase from the center towards the crystal rim, which (at sufficiently low pull rates) results in a vacancy excess in the center, while Si interstitials dominate at the crystal rim, as indicated in Fig. 5.9. Figure 5.10 illustrates how the radial position of the crossover between ξ_{tr} and $V/G(r)$ and hence the boundary between the void and L-pit regions is shifted when V is varied.

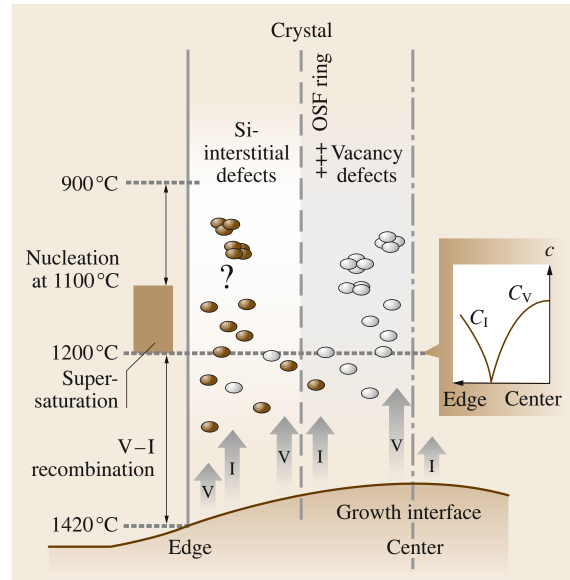

Fig. 5.8 Schematic picture of the incorporation of vacancies (V) and Si interstitials (I), respectively, into the growing crystal. The *insert on the right* shows the radial variation of the remaining species after V–I recombination has ceased and supersaturation starts

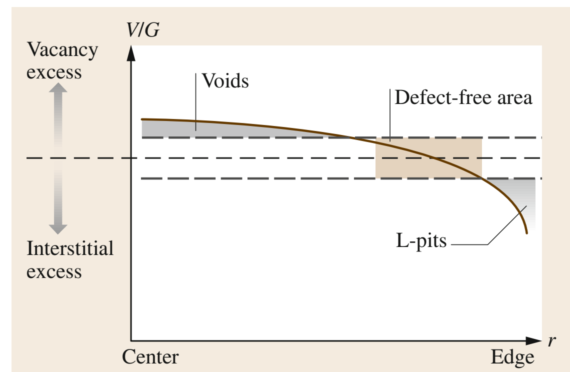

Fig. 5.9 Schematic radial variation in defect types as a function of the radial variation of V/G

The exact value of ξ_{tr} is still under discussion, because G has to be taken directly at the interface where the thermal field in the crystal changes very rapidly [5.35, 76]. Therefore, it has not been possible to accurately measure G at the growth interface [5.77]. Fortunately, computer simulations with sufficiently refined meshes permit a rather accurate calculation of G. Based on these calculations, a value of $0.13\,mm^2\,min^{-1}\,K^{-1}$ has been determined from growth experiments, with hot zones of different Gs [5.33], which, however, is currently debated again.

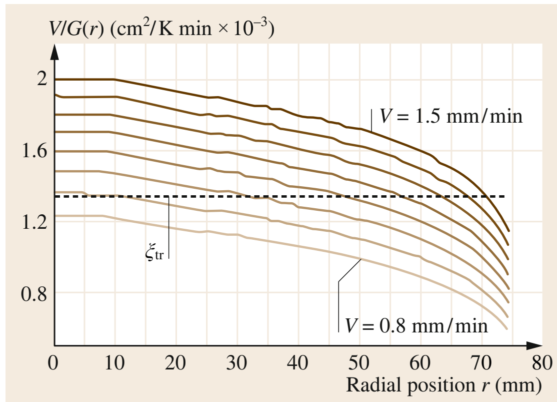

Fig. 5.10 Radial variation in the crossover between the transition value ξ_{tr} and $V/G(r)$ as function of decreasing pull rate V

It should be noted that the above behavior is probably unique to silicon as it stems from the peculiar phenomenon that the vacancy and Si interstitial equilibrium concentrations in crystalline silicon are very similar, but C_V^{eq} is slightly higher than C_I^{eq}, although the diffusivity of Si interstitials exceeds that of vacancies at the melting point. In addition, the quantitative relationship between the relevant parameters which allows the changeover in defect behavior to occur in accessible growth rate regimes is quite astonishing. The time-dependent behaviors of the point defect concentrations are determined by the species conservation equations [5.78]

$$\frac{DC_I}{Dt} = \nabla\left[D_I(T)\nabla C_I - \frac{D_I(T)C_I Q_I^*}{k_b T^2}\nabla T\right] - k_{IV}\left(C_I C_V - C_I^{eq} C_V^{eq}\right) - \frac{\partial}{\partial t}\int_2^{\infty} n f_I(n,r)\,dn\,, \quad (5.2)$$

where Q_I^* is the reduced heat of transport for Si interstitials, which describes the rate of material flow due to a temperature gradient. A similar expression applies for vacancies (just exchange the I and V notations). The substantial derivative $D/Dt = [\partial/\partial t + V(\partial/\partial z)]$ is defined here as the rate of change of species concentration at a point moving with the velocity (V) of the advancing growth interface. This term relates to the incorporation of species due to convection. The first term on the left-hand side accounts for Fickian diffusion and the second for thermodiffusion. The last term represents the loss of point defects into their aggregates of all possible sizes. This term can be neglected as long as the supersaturation of the surviving species has not increased to the point where cluster nucleation starts. A detailed analysis also reveals that thermodiffusion has no detectable impact. Hence, the simple picture drawn above – which only takes into account convection and Fickian diffusion – is quite reasonable. Based on these simplifications, the incorporated vacancy concentration can be calculated from a simple expression [5.76, 79]

$$C_V(r) \approx \left[C_V^{eq}(T_m) - C_I^{eq}(T_m)\right]\left(1 - \frac{\xi_{tr}G(r)}{V}\right). \quad (5.3)$$

This expression is also applicable to Si interstitials (at $V/G < \xi_{tr}$). It then defines the incorporated Si interstitial concentration C_I with a minus sign.

If V/G approaches ξ_{tr}, then the vacancy and Si interstitial fluxes become equal and both species are annihilated by V–I recombination. Thus, the incorporated V and I concentrations are negligible and no aggregates can form. This particular condition must be met for the growth of so-called perfect and *defect free* silicon, respectively.

Based on the picture outlined above, one would expect to be able to grow crystals which are I-rich in the center and V-rich near the surface by simply engineering the hot-zone and the process conditions in such a way that G is higher in the center than at the rim of the growing crystal (Fig. 5.11). Surprisingly, respective experiments which were carried out some years ago showed that, under such conditions, vacancy aggregates can still prevail in the center and interstitial clusters at the periphery of the crystal [5.80]. The authors explained these findings by the effect of thermo-mechanical stress during growth on the solubility of native point defects by noting that compressive stress increases the solubility of V_s and vice-versa for I_s. As a consequence, the critical value of V/G, where vacancies and interstitials annihilate each other, be-

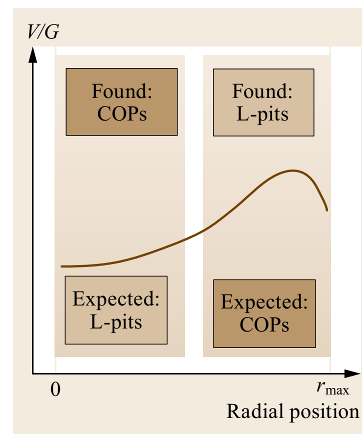

Fig. 5.11 Radial variation of V/G for a special hot zone with compressive stress in the crystal center and tensile stress at the periphery of the growing crystal. Comparison of expected and experimentally found defect behavior

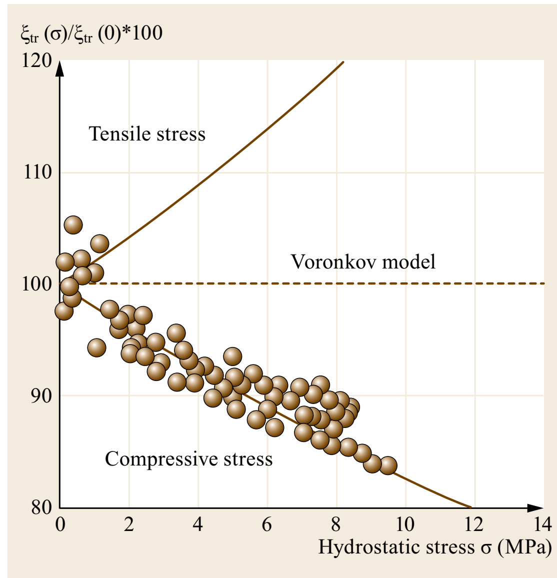

Fig. 5.12 Dependence of $\xi_{tr}(\sigma)/\xi_{tr}(0)$ on tensile and compressive stress in the growing crystal. *Open circles* show the data of *Nakamura* after scaling the hydrostatic stress to account for the differences in elastic parameters used. (After [5.44, Fig. 1], [5.80])

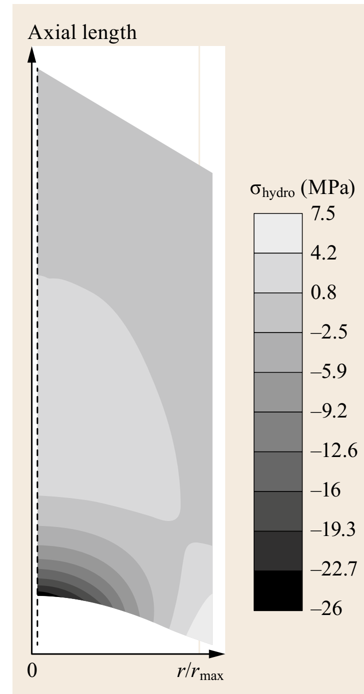

Fig. 5.13 Distribution of stress in a growing crystal which has a similar radial variation of V/G as in Fig. 5.11. However, the stress in the growing crystal is engineered in such a way that *defect free* silicon is obtained

comes a function of the thermo-mechanical stress in the vicinity of the growth interface (5.1). Figure 5.12 shows how $\xi_{tr}(\sigma)/\xi_{tr}(0)$ depends on hydrostatic stress according to [5.80].

The dependence is obtained from the classical expression for $\xi_{tr}(0)$ (5.1) by adding the effect of hydrostatic stress to the formation enthalpy of point defects i. e., by adjusting the volume change due to point defect creation using the same value for both I's and V's for simplicity and neglecting the effect of stress on point defect diffusivity. It should be noted that a more accurate solution is obtained if the diffusion-convection-reaction problem is solved in the full crystal which is especially important for strongly curved interfaces.

Figure 5.13 depicts the distribution of hydrostatic stress and crystal interface shape for a 300 mm crystal where the radial variation of V/G is similar to that of Fig. 5.11, but the thermo-mechanical stress is engineered to balance V/G so that *defect free* silicon can be obtained [5.80]. There is quite large compressive stress in the crystal center and several times smaller tensile stress near the triple point.

The effect of stress on the formation energy of point defects was already discussed by *Tanahashi* et al. [5.81], before the above experiment was carried out, but their estimates were far too low to explain the findings of [5.80]. Recently, *Nakamura* et al. [5.44] published a new set of data showing the dependence of $\xi_{tr}(\sigma)/\xi_{tr}(0)$ on hydrostatic stress. They are in good agreement with Fig. 5.12, if one corrects the effect of the different elastic parameters used in both publications. For a more detailed analysis including extensive atomistic simulations, we refer to the recent literature [5.45, 82, 83].

5.3.3 Theoretical Model: Aggregation of Intrinsic Point Defects

Due to the technological dominance of vacancy-rich silicon, previous theoretical investigations of defect aggregation have mainly focused on the formation of voids. In addition, it was also easier to verify the theoretical results for vacancy aggregation because voids are not obscured by the secondary defect generation that occurs for L-pits.

From Fig. 5.14, it can be seen that, for a standard growth process, the V-supersaturation already begins to build up at around 1200 °C [5.84], which is well above the experimentally determined nucleation temperature of voids ($\approx 1100\,°C$). Thus, the supersaturation C_V/C_V^{eq} necessary to nucleate voids is appreciable, ≈ 10 [5.78], as estimated from Fig. 5.14. This fact also allows us to decouple the phase where V–I recombination is the major vacancy loss mechanism from the phase where nucleation dominates the vacancy loss, so that one can assume that the cluster formation starts with a fixed concentration which can be cal-

culated from (5.3). For special growth processes that are designed to minimize or even eliminate voids, the starting vacancy concentration after V–I recombination is so small that the beginning of supersaturation (and hence void nucleation) occurs at notably lower temperatures [5.79].

The first vacancy aggregation calculations were performed with a model that was originally developed to simulate oxygen precipitation [5.64, 85]. For the formation of small clusters (less than 20 vacancies), the kinetics are described by chemical rate equations; for larger clusters, the rate equations are expanded into a continuum formulation that yields a single Fokker–Planck equation. The void shape is assumed to be spherical. Input data are the computed temperature field, which can be quite accurately calculated using commercially available standard codes, and the surviving vacancy concentration after V–I recombination has ceased. Besides the physical properties of the vacancies and Si interstitials, the surface energy must also be known, which is estimated to be around 950 erg/cm^2.

As can be seen from Fig. 5.14, the computer simulations yield a nucleation temperature of around 1100 °C, which agrees fairly well with the experimental results. The prediction of the correct aggregation temperature has been a matter of discussion. With the above input data, one ends up with a far lower aggregation temperature than those observed [5.86, 87]. The main reason for this is that the nucleation process does not start as a small octahedral void as previously assumed, but rather as an *amorphous cloud* of vacancies which, after some time, relaxes into an octahedron with (111) facets [5.88]. Proper modeling of this initial nucleation process with atomistic calculations does indeed shift the calculated aggregation temperature into the experimentally observed range.

The results in Fig. 5.14 also demonstrate that a higher cooling rate obviously decreases the nucleation temperature. The origin of this effect is the increased supersaturation, which builds up because there is less time for vacancy consumption. Due to the shift in the nucleation temperature, the residual vacancy concentration after void formation remains higher for fast cooling rates than for slow cooling. This has an important effect on the nucleation of oxygen precipitates, as the latter is strongly enhanced by a higher free vacancy concentration. Figure 5.15 illustrates the evolution of the void density/size distribution during the nucleation period. It is apparent that the maximum of the distribution is shifted to larger void sizes not only due to the growth of the previously nucleated voids, but also due to the fact that the newly nucleated clusters have a larger size. The latter effect results from the decreased supersaturation with higher void density, which, in turn, increases

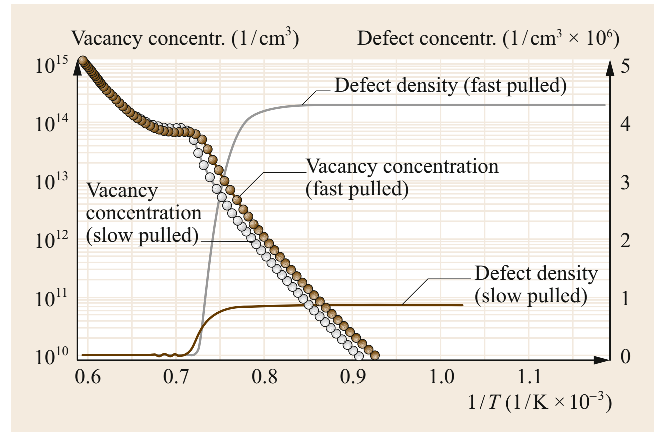

Fig. 5.14 Simulated variation in the vacancy concentration in growing crystals as a function of temperature for rapidly and slowly cooling growth processes. The density of voids nucleated at around 1100 °C and below is shown on the *right scale*

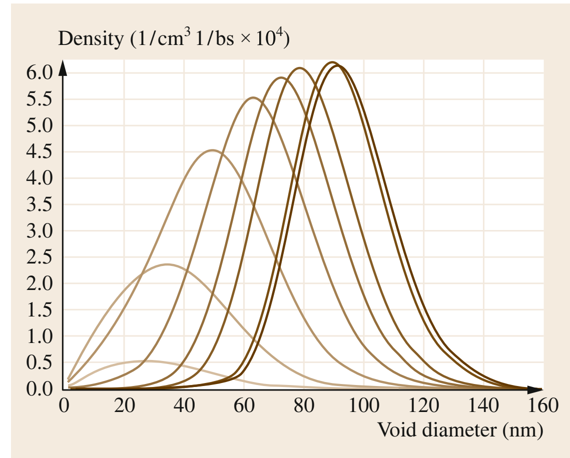

Fig. 5.15 Simulated evolution of the void density–size distribution at various temperatures of the growing crystal. The temperature difference between each curve is 4 K

the critical radius for stable nuclei. Thus, only increasingly large clusters can nucleate towards the end of the nucleation period.

As depicted in Fig. 5.16, a fast cooling rate decreases the cluster size but increases their density and vice versa, which correlates well with the experimental data. The reason for this is the above-mentioned higher supersaturation at fast cooling rates, which entails a larger nucleation rate. The higher cluster density then effectively lowers the residual vacancy concentration. The clusters, however, have no time to grow and so remain small.

A similar effect is obtained when the initial vacancy concentration before the onset of nucleation is

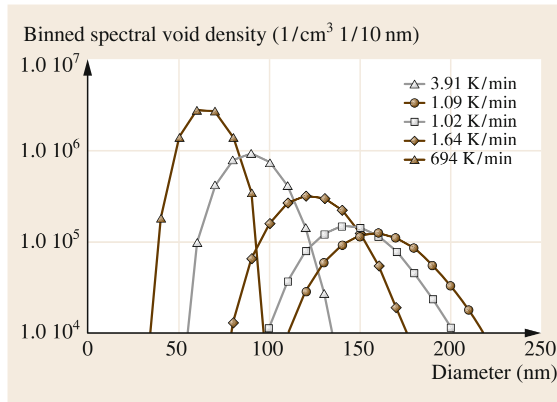

Fig. 5.16 Simulated density/size distributions of voids for growth processes with different cooling rates

reduced [5.89]. A lower vacancy concentration causes a downward shift in the nucleation temperature, where the vacancy diffusivity is lower. As a consequence, they need more time to diffuse to sinks, which in turn drives up supersaturation and so more clusters of a smaller size are formed again. The behavior of the size distribution as a function of the initial vacancy concentration gives a simple explanation for the experimentally found radial variation in the void size distribution in Fig. 5.7. As the initial vacancy concentration decreases towards the crystal rim (Fig. 5.17), the average size of a void shrinks but void density grows. Thus, the density of small voids is low in the center, but increases towards the crystal rim until the vacancy concentration drops below a critical value, where the average void size is below the detection limit. On the other hand, the number of large voids shrinks with decreasing vacancy concentration. Therefore, the density of large COPs is highest in the center. This behavior is also fairly well reproduced by simulation (Fig. 5.18).

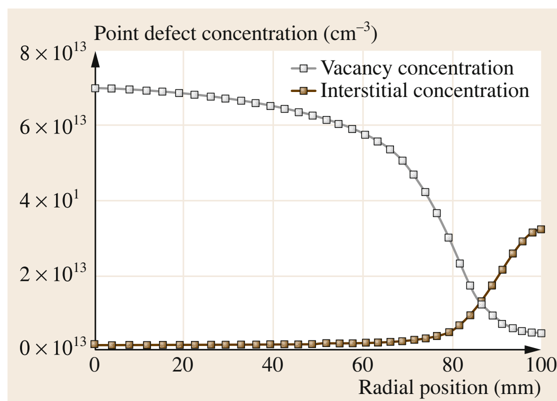

Fig. 5.17 Simulated radial variations in the vacancy and Si interstitial concentrations, respectively. (After [5.70])

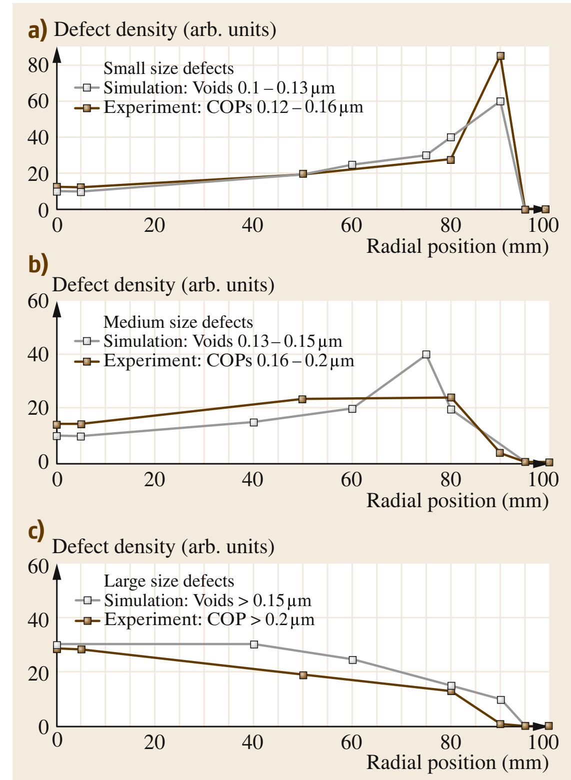

Fig. 5.18a–c Simulated radial variation in the density/size distribution of voids and comparison with experimental data. (After [5.70])

A simple expression that predicts a void density proportional to $q^{3/2}C_V^{-1/2}$ ($q=$ cooling rate, $C_V=$ initial vacancy concentration before nucleation starts) has been derived by *Voronkov* et al. [5.68]. This formula is obviously in excellent agreement with the experimental results (Fig. 5.19). A deviation from the above expression was reported for detached crystals, where significantly higher cooling rates can be achieved (2–70 K/min) [5.90]. In the latter case, this discrepancy was tentatively explained by a suppression of voids in favor of enhanced formation of oxygen precipitates at high cooling rates (> 40 K/min) [5.91]; in other words, so-called *oxide particles* nucleate at around 1100 °C rather than voids.

The $C^{-1/2}$ dependence is more difficult to verify experimentally because a change in the initial vacancy concentration entails a change in the nucleation temperature and so temperature-dependent parameters like diffusivities and equilibrium concentrations must be adjusted. Most of the current aggregation models do not consider the oxidation of the inner void surface, which stops void growth before the vacancies are essentially depleted. This has less impact on the void size

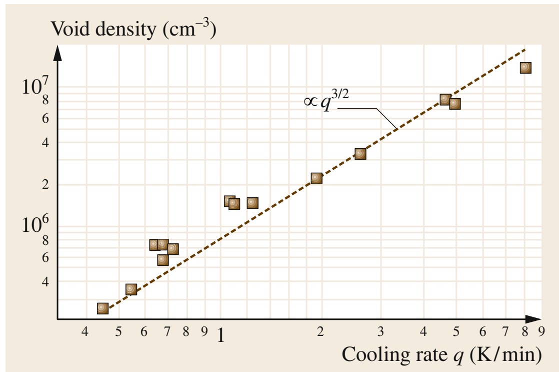

Fig. 5.19 Void density as derived from GOI measurements as a function of cooling rate of the growing crystal. The *straight line* relates to predictions of the $q^{3/2}$ law

distribution but considerably affects the residual vacancy concentration and therefore oxygen precipitation (Sect. 5.4).

The occurrence of double voids is still under discussion. One attempt to explain this phenomenon is based on a partial oxidation of the (111) facets during void growth, which allows the incorporation of further vacancies at the unoxidized residual facet surface [5.92].

5.3.4 Effect of Impurities on Intrinsic Point Defect Aggregation

The influence of impurities on the aggregation of intrinsic point defects has been widely investigated. It was found that many of them can notably modify the defect density and size which is of great technological importance. Many attempts have been made to explain the specific mechanisms. However, a unified theoretical approach has not been achieved. This is also due to the fact that the observed effects occur at concentrations which vary over many orders of magnitude.

Nitrogen

Codoping of silicon crystals with nitrogen is of considerable relevance in technical applications, as nitrogen already has a massive impact on point defect aggregation at very low concentrations. It has long been known to simultaneously suppress interstitial- and vacancy-related defects – A-swirls and D-defects/voids, respectively [5.93] – in floating zone (FZ)-grown crystals. The nitrogen concentrations required are very low ($< 2\times10^{14}$ at/cm^3) and were found to be in the same range as the surviving residual intrinsic point defect concentrations. Owing to the low nitrogen concentration, adverse effects of nitrogen codoping are technically insignificant. Well known is the formation of nitrogen related thermal donors after neutron transmutation doping which, however, can be handled by properly annealing the neutron irradiated ingots [5.94]. Consequently, all FZ grown silicon crystals are nitrogen codoped, today.

In the case of Czochralski (CZ)-grown silicon, nitrogen has been an undesirable dopant in the past, because it enhances the formation of oxidation-induced stacking faults (OSF) [5.95]. As the nitrogen concentration increases, the OSF ring widens [5.96] until it extends over the entire crystal diameter. In addition, due to the comparatively high oxygen concentration ($3–8\times10^{17}$ at/cm^3), the desirable defect suppressing effects of nitrogen are largely offset by the interaction of nitrogen and oxygen [5.97]. However, nitrogen still has a notable effect on the defect size: the higher the nitrogen concentration, the lower the defect size [5.18, 98]. This effect is important, because a small defect size is highly favorable for defect annealing [5.16]. It was further found that nitrogen not only reduces the defect size but also systematically changes the void morphology from octahedron to platelet and, finally, to rods or even rod clusters with increasing concentration (Fig. 5.20) [5.99]. Nitrogen doping has gained additional interest as it also strongly enhances oxygen precipitation [5.100–102] which can be used to improve the efficiency of gettering of metallic contaminants in low thermal budget device processes [5.103, 104].

Unfortunately, quantitative data on the chemical and physical properties of nitrogen in silicon are rare. Experimentally, it was found that nitrogen exists as N–N dimers in as-grown silicon [5.105], which has a diffusivity three orders of magnitude higher than oxygen at 1100 °C [5.106]. These diffusion experiments indicate that the N–N dimer is stable up to at least 1270 °C [5.107], which is in line with first-principles

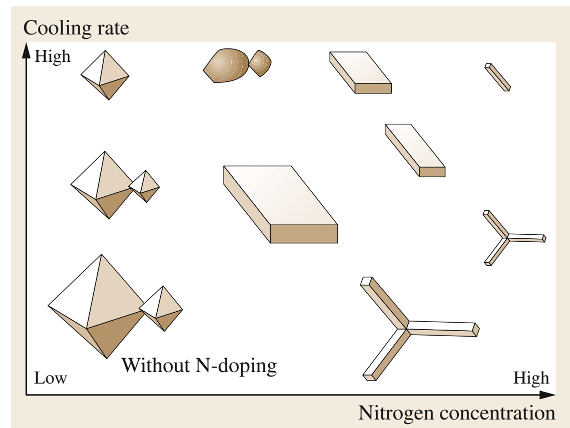

Fig. 5.20 Variation in void morphology as a function of nitrogen concentration and cooling rate of the growing crystal. (After [5.99])

calculations of the N–N dimer configuration [5.108–110]. In contrast with the nitrogen molecule, the N–N dimer in silicon does not have any direct bonds between the two neighboring nitrogen atoms. Experiments with nitrogen-implanted silicon samples heated to melt temperature by a laser pulse and subsequently quenched to room temperature proved that roughly 10% of the nitrogen can be frozen on substitutional sites as single nitrogen atoms [5.111, 112]. The fact that substitutional nitrogen is generally not observed in regularly cooled samples suggests that substitutional nitrogen is not stable in silicon at lower temperatures [5.113].

As the nitrogen concentration needed to suppress A-swirl and D-defects is in the same range as the intrinsic point defect concentration before aggregation, it was suggested that nitrogen directly interacts with vacancies (V) and Si interstitials (I) and thus prevents their aggregation [5.114, 115]. One model proposes that the storage of vacancies in impurity complexes would gradually shift the transition value ξ_{tr} of V/G to higher values which, in turn, would explain the shrinkage of the void region with increasing nitrogen content [5.116]. On the other hand, the model also seems to imply that the A-swirl region simultaneously expands toward the crystal center, which is in conflict with experimental results. In particular, the Li-drift experiments of *Knowlton* et al. [5.117] proved that, despite the suppression of detectable COPs, the extent of the vacancy-rich region does not change due to nitrogen doping. Other attempts are based on the reduction of vacancy diffusivity due to the vacancy–nitrogen interaction [5.118] or on increasing the reaction barrier to vacancy absorption at the void interface [5.119]. However, the fact that nitrogen doping has no impact on the inner oxide layer growth of the voids [5.99] does not support the notion that nitrogen modifies the properties of the void interface. None of these proposals gives any explanation for influence of nitrogen on Si interstitial aggregation.

First-principles calculations by *Sawada* et al. [5.108] and *Kageshima* et al. [5.109] have shown that the N–N dimer can form stable N_2V and N_2V_2 complexes, the latter being more stable due to a larger enthalpy of formation. Based on these results, it has been proposed that the vacancy aggregation is suppressed by the reaction

$$\text{I)}\quad N_2 + V \leftrightarrow N_2V\,,$$

whereas the formation of Si interstitial agglomerates is prevented by the reaction

$$\text{II)}\quad N_2V + I \leftrightarrow N_2\,.$$

Nitrogen is not likely to be incorporated as a N–N dimer into the crystal. This is concluded from the experimental fact that nitrogen does not evaporate from the silicon melt and so it must be strongly bound to silicon atoms, which is not possible for a nitrogen molecule. It was therefore proposed that single nitrogen atoms are incorporated on interstitial (N_I) as well as substitutional sites (N_s) at the growth interface [5.120]. Behind the growth interface, the highly mobile interstitial nitrogen atoms then quickly form N–N dimers via $N_I + N_I \leftrightarrow N_2$ and nitrogen-vacancy complexes via $N_I + N_s \leftrightarrow N_2V$ inside the crystal. A ratio of $[N_I]:[N_S] = 7:1$, which corresponds to 12% of the nitrogen at substitutional sites, has been determined from FZ crystals grown with various nitrogen contents. This is in good agreement with the above-mentioned experimental findings for substitutional nitrogen. As vacancies and Si interstitials have very similar concentrations at the melting point, reactions (I) and (II) mainly act as an additional V–I recombination path during crystal cooling, with only marginal impact on the levels of N_2 and N_2V. However, when recombination is complete and the vacancies or the Si interstitials have been wiped out, reaction (I) or (II) prevents the aggregation of the surviving species. Using this model, it has been possible to determine the radial variations of vacancies and Si interstitials in FZ crystals before the onset of defect aggregation [5.120]. This was achieved by measuring the radial extension of the COP and A-swirl region as a function of the nitrogen concentration. The result is in excellent agreement with theoretical predictions (Fig. 5.21). Surprisingly, the experimental data could not be fitted by assuming that the formation of N_2V_2 complexes prevails, as predicted by theoretical calculations. It is not clear whether the reaction to N_2V_2 is hampered by a high-energy barrier.

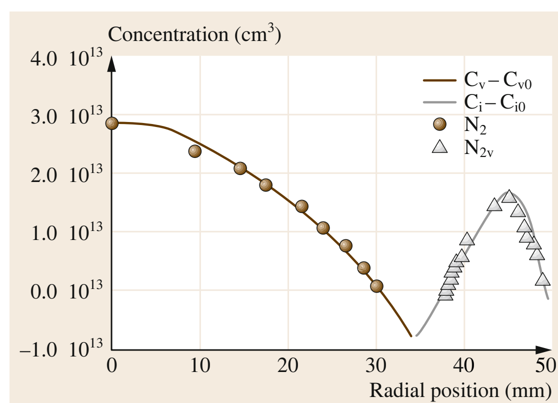

Fig. 5.21 Radial vacancy and Si interstitial distributions as derived from a FZ crystal grown with an axially varying nitrogen concentration. $C_{V0} = 8.8 \times 10^{12}\,\text{at/cm}^3$ and $C_{I0} = 7.7 \times 10^{12}\,\text{at/cm}^3$. The *solid* and *dashed lines* refer to simulation results. (After [5.120])

None of the above mentioned models can explain why the effect of nitrogen on defect aggregation is strongly diminished in CZ crystals. It is clear that the well-known interaction between nitrogen and oxygen, which results in the formation of N_xO_y complexes [5.121], is probably the origin of the vanishing nitrogen effect. However, it is also known that, despite oxygen levels of 5-6 $\times 10^{17}$ at/cm^3, ample unreacted nitrogen is left in oxygen- and nitrogen-doped as-grown crystals to suppress defect aggregation [5.122]. It is therefore necessary to look for a mechanism that significantly reduces the concentration of free nitrogen dimers at the nucleation temperature of voids and L-pits, but reestablishes their concentrations at lower temperatures. As the experimentally confirmed N_2O complex is only stable up to about 700 °C [5.121, 123], it has been proposed [5.120] that nitrogen reacts with oxygen at high temperatures according to

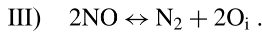

III) $2NO \leftrightarrow N_2 + 2O_i$.

The existence of the NO complex has been theoretically predicted by *Gali* et al. [5.124] and, more recently, has also been experimentally confirmed [5.125, 126]. It has a similar structure to the N_2 complex but with a smaller binding energy. Due to the large excess of oxygen over nitrogen, it has been assumed that the equilibrium of reaction (III) is on the left-hand side near the melting point and so very little N_2 is available. As the temperature decreases, the equilibrium gradually shifts to the right-hand side and more and more N_2 is generated. If the temperature at which N_2 starts to develop in sufficient quantities is below the vacancy aggregation temperature, the formation of voids is not suppressed. If the N_2 formation temperature is above the vacancy aggregation temperature, void formation depends on how much N_2 is available in relation to the vacancy concentration at the void nucleation temperature. The higher the N_2 formation temperature, the more N_2 is available to reduce the number of vacancies by reaction (I). According to reaction (III), the formation temperature of N_2 should increase with lower oxygen and higher nitrogen concentrations. Lower free vacancy concentrations and therefore lower aggregation temperatures result in voids of smaller size but higher density, in agreement with the experimental findings.

After void nucleation, the free vacancy concentration drops rapidly and the above reaction (I) reverses, giving $N_2V \rightarrow N_2 + V$, which slows down the decay of free vacancies. Thus, the N_2V-complex acts as an interim reservoir for vacancies – its formation before void formation removes vacancies and its dissociation after void formation releases them again [5.96]. In conjunction with the lower vacancy aggregation temperature,

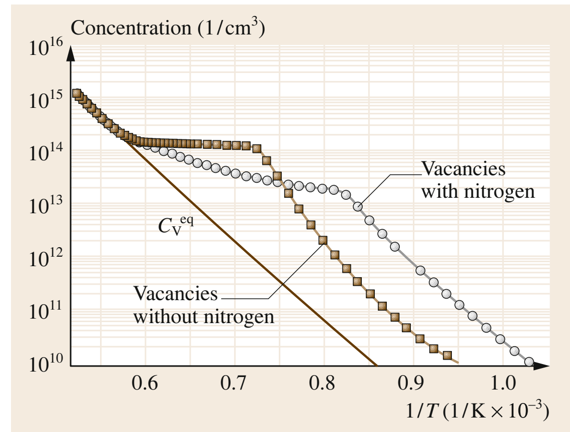

Fig. 5.22 Simulated variations in the vacancy concentration as a function of temperature for a nitrogen-doped and an undoped crystal

this results in a notable increase in free vacancy concentration during this cool-down phase compared to nitrogen-free material (Fig. 5.22). As free vacancies are known to strongly favor the nucleation of oxygen precipitates, the latter effect gives a simple explanation for the observed strong enhancement of oxygen precipitation in nitrogen-doped CZ crystals (Sect. 5.4).

The remarkable variation in the void morphology as a function of the nitrogen content is still under discussion. A similar change in morphology is also known for oxygen precipitates. In this case, the effect can be interpreted in terms of the balance between the relaxation energy of the lattice strain and the interfacial energy. However, TEM investigations do not reveal any lattice strain around voids, and so another mechanism is required to explain the varying void morphology.

Boron

Boron doping affects the intrinsic point defect aggregation in a similar way to nitrogen doping, but much higher concentrations are required [5.127]. These high concentration are technologically relevant as highly boron doped wafers are widely used as substrates for epitaxial layers in the electronic industry. It was found that the COP region as well as the diameter of the OSF ring starts to shrink when the boron content exceeds roughly 5 $\times 10^{18}$ at/cm^3 (Fig. 5.23). In contrast with nitrogen, OSF formation is not enhanced and the width of the OSF ring remains unchanged with increasing boron concentration. At around 10^{19} at/cm^3, the COPs and the OSF ring disappear in the center of the crystal. More recently, it was reported that L-pits are also suppressed in the same concentration range [5.128] which is in line with the well known defect-free quality of pp + epi wafers [5.62] (Sect. 5.3.1).

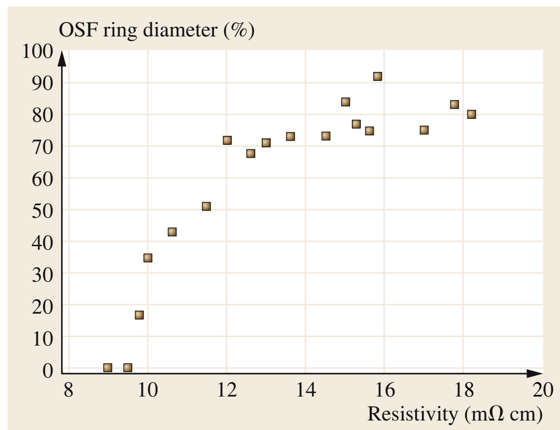

Fig. 5.23 Variation in the OSF ring diameter as a function of the boron concentration. (After [5.129])

Dornberger et al. [5.69] suspected that changes in the equilibrium concentrations and diffusivities of intrinsic point defects in the presence of high boron concentrations would modify the transition value ξ_{tr} of the parameter V/G as a function of the boron content. *Voronkov* and *Falster* [5.87] also proposed a modification of equilibrium concentrations as a result of the shift in the Fermi level due to the high boron concentration. Based on this approach, the latter authors calculated a shift in the transition value ξ_{tr} which would account for the observed shrinkage of the void region. However, *Vanhellemont* et al. recently carried out ab initio calculations which demonstrated that vacancies at the melting temperature of silicon are neutral independent of the position of the Fermi level [5.130]. As with nitrogen doping, the ξ_{tr} shift entails the simultaneous appearance of L-pits in the outer crystal region and a shrinking void region, which is in conflict with experimental results of boron doped crystals, as well. Another attempt by *Sinno* et al. [5.131] considers reversible reactions between boron and intrinsic point defects, in particular self-interstitials. The formation of BI and B_2I complexes consumes self-interstitials which would otherwise be annihilated by recombination. As recombination consumes the remaining self-interstitials, BI and B_2I start to dissociate again according to le Chatelier's principle. As a result, the self-interstitial concentration increases, which shifts the point defect balance towards the intersitial-rich side, causing the void region to shrink. No comment is made about whether or not the model is also able to account for the suppression of L-pit formation by storing supersaturated self-interstitials in boron complexes. Recently, *Sueoka* et al. presented a model which considers the variation of formation energies of intrinsic point defect around dopant atoms and, thus, the change of equilibrium concentrations of vacancies and Si interstitials in dependence on the dopant concentration [5.46]. In case of boron, their results correctly predicted the behaviour of the void region as a function of the boron concentration, but the simultaneous suppression of L-pits was not reproduced. They suspected that, in contrast with vacancies, the Fermi level effect cannot be neglected for self interstitials which would turn them into positively charged species [5.132]. The suppression of interstitial clusters could then be explained by the Coulomb repulsive force. However, the debate on whether or not Si interstitials are charged or neutral is not yet settled.

Carbon

Carbon doping is also known to impact intrinsic point defect aggregation. It has been reported that the void region in the crystal center disappears upon carbon doping [5.59, 133], while the region of Si interstitial aggregates is widened; in other words, carbon does not inhibit the formation of L-pits/A-swirl. This behavior appears to be in line with the model put forward in [5.116], which predicts an upward shift of ξ_{tr} for carbon doping and, in turn, an enlargement of the interstitial-rich region.

It was also found that carbon doping reduces the grown-in defect size [5.99, 134]. Although the size reduction is appreciable, the morphology of the voids is not changed, in contrast to the consequences of nitrogen doping. Only a tendency towards multiple void formation was observed. The thickness of the inner oxide layer was found to be similar to that of undoped crystals, which indicates that carbon doping has no influence on the growth of the inner oxide layer. In more recent studies, it was reported that the morphology and size of Si interstitial aggregates changes with increasing carbon concentration [5.128, 135]. The L-pit, which is a local network of dislocation loops, turns into a globular Si interstitial aggregate, probably a stacking fault of Si interstitials. In addition, the density of these defects is notably increased with the carbon content. As with boron, the effect on defect aggregation is only seen at significantly higher concentrations ($\approx 1\times10^{17}$ at/cm^3) than for nitrogen. The above model of *Sueoka* et al. was also applied to carbon and showed qualitative agreement with the experimental findings [5.46].

At higher concentrations, carbon is known to enhance oxygen precipitation too [5.136, 137]. As carbon predominantly resides on substitutional sites, it is very unlikely that, as in the case of nitrogen doping, a higher residual vacancy concentration is responsible for the stronger oxygen precipitation. On the other hand, the small carbon atom exerts a local tensile strain on the surrounding lattice and attracts Si interstitials to form C_xI_y complexes. Thus, Si interstitials ejected into the

lattice by growing oxygen precipitates are effectively removed and, in turn, further precipitate growth is not retarded by a build-up of Si interstitial supersaturation. The enhanced oxygen precipitation may also be related to heterogeneous nucleation at small carbon aggregates [5.138].

Antimony, Arsenic and Phosphorus

In recent years, the effect of n-type dopants in high concentrations like antimony, arsenic and phosphorus have been been investigated in detail [5.128, 139–142]. Similar to boron, highly n-doped wafers are used as substrates for epitaxial layers which are mainly needed for high power devices. In contrast with highly boron doped crystals, all of these n-dopants expand the void region with increasing concentration. e.g., crystals, which are grown under conditions that make them Si interstitial rich (L-pits), are transformed into vacancy rich with strong void formation upon a Sb doping level of 3×10^{17} at/cm^3 [5.139]. This is also in line with older measurements on Sb doped floating zone grown crystals where the defect behaviour was shifted from Si interstitial rich (A-swirl) to vacancy rich (D-defects) by Sb doping [5.143]. The void density increases with higher dopant concentrations. However, beyond a certain critical concentration, the void density sharply drops and no defects are observed anymore. The critical level obviously depends on the dopant and is highest for phosphorus and lowest for antimony (Fig. 5.24). The void density is rather uniform across the crystal diameter and also disappears uniformly beyond the critical dopant concentration. The morphology of the voids changes with the n-dopant [5.142]. For Sb-doping, single voids were observed, only, while, in case of P-doping, one quarter of the voids was detected as double voids. More than 50% double voids were found in As-doped crystals. Unlike nitrogen, carbon and boron, oxygen precipitation is not notably affected by the n-dopants, but is rather similar to the behaviour of lightly doped wafers.

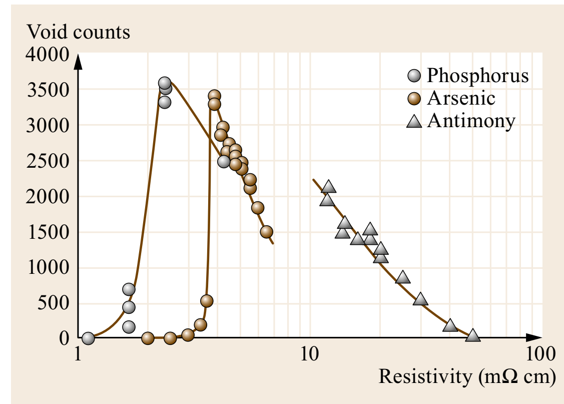

Fig. 5.24 Void counts in dependence of the resistivity for P-doped (*grey circles*), As-doped (*brown circles*) and Sb-doped crystals (*grey triangles*). (After [5.142])

All proposed models explain the observed effects by assuming a shift of ξ_{tr} to lower values. While *Voronkov* et al. [5.144, 145] attribute the shift of ξ_{tr} to vacancy and Si interstitial trapping by the dopants, respectiviely, and can also reproduce the sharp drop of the void density beyond the critical dopant concentration [5.141], *Sueoka* et al. again apply their above mentioned model predicting a change of the formation energy of vacancies and self interstitials in the presence of n-dopants which results in a similar shift of ξ_{tr} [5.46].

5.4 Formation of OSF Ring

The ring-like distributed OSFs are oxygen precipitates with platelet shapes that grow particularly large at the edge of the void region, and exceed a critical size necessary to create stacking faults during subsequent wafer oxidation there [5.146]. The critical radius of the grown-in platelets is ≈ 70 nm. The formation of OSFs can be suppressed if the cooling rate of the growing crystal is increased (this means, for example, that OSFs are not found in oxygen-doped FZ crystals [5.129] which have very high cooling rates) or if the oxygen content is decreased.

The peculiar ring-like distribution is a consequence of the well-known strong enhancement of oxygen precipitation by vacancies [5.38, 147]. The reason for this is that the absorption of vacancies allows the oxygen precipitate, which occupies twice as much volume as the corresponding silicon lattice, to nucleate and grow without building up notable strain energy. As will be described below, the radially inhomogeneous oxygen precipitation is a consequence of a substantial radial inhomgeneity of the free vacancy concentration in contrast to the rather flat radial profile of oxygen.

The vacancy concentration, as pointed out previously, has its maximum at the center of the growing crystal after V–I recombination has ceased (Fig. 5.25). Therefore, the critical supersaturation for void formation is first reached at the crystal center at relatively high temperatures. Hence, the free vacancies are quickly consumed in this area. As the crystal cools, voids are also nucleated in the regions of lower initial vacancy

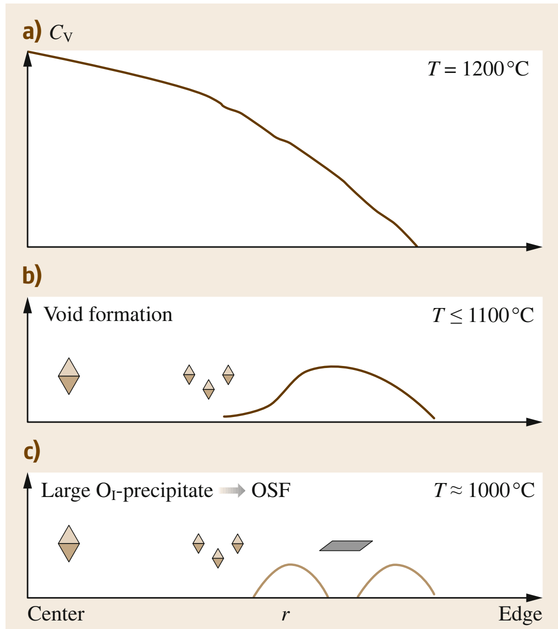

Fig. 5.25a–c Schematic evolution of the radial vacancy profile and accompanying void and large O_I-precipitate formation at decreasing temperatures

concentration, meaning that vacancy consumption then also occurs further away from the crystal center. As the removal of vacancies is enhanced at higher temperatures, where the diffusivity is large, the radial vacancy distribution finally drops to a minimum in the crystal center, and the maximum of the residual vacancies gradually moves toward the V/I boundary upon further cooling. Because of this shifted vacancy maximum, the first oxygen aggregates nucleate close to the V/I boundary on the vacancy-rich side. The relatively high nucleation temperature at this position results in larger sizes but lower densities for the corresponding grown-in oxygen precipitates compared to those nucleated at lower temperatures away from the V/I boundary. Consequently, they preferentially reach the critical size for OSF formation during subsequent wafer oxidation. At sufficiently fast crystal cooling rates, the oxygen precipitates are nucleated at higher densities but smaller sizes and cannot grow to the critical size. Thus, OSF formation is prevented, in agreement with experimental findings. The same density/size effect is obtained if the oxygen content is lowered – similar to the behavior of voids – and so OSFs are also suppressed.

The nucleation of the first oxygen precipitates quickly results in the depletion of residual vacancies in their neighborhood. Thus, the previous vacancy maximum at the V–I boundary is then converted into a pronounced minimum which suppresses further nucleation in this area. As a result, two vacancy peaks with a region of large oxygen precipitates in-between is frozen in as the crystal cools down to room temperature (Fig. 5.25). Later on, when the wafers are subjected to further heat treatments, such as a nucleation step at 780 °C followed by a growth step at 1000 °C, new oxygen precipitates with high density are preferentially nucleated at the radial positions of the two remaining vacancy maxima. This results in a distinct profile for the interstitial oxygen concentration after these heat treatments. In the radial band where the large precipitates and the OSF ring are located, the interstitial oxygen concentration is only slightly reduced because further nucleation of precipitates during wafer heat treatment is suppressed there and the comparatively low density of precipitates does not consume much of the interstitial oxygen. On the other hand, the high density bands at the locations

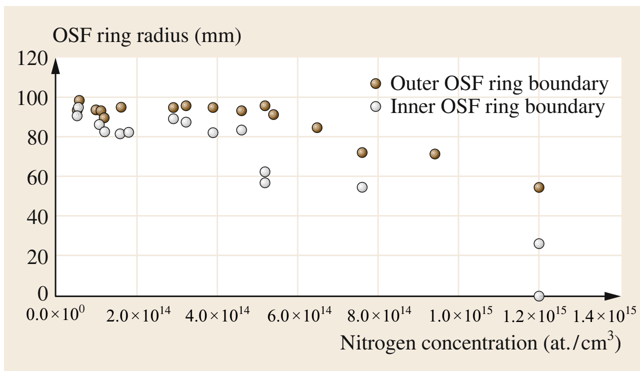

Fig. 5.26 Variations of the outer and inner OSF ring boundaries as a function of the nitrogen concentration. (After [5.96])

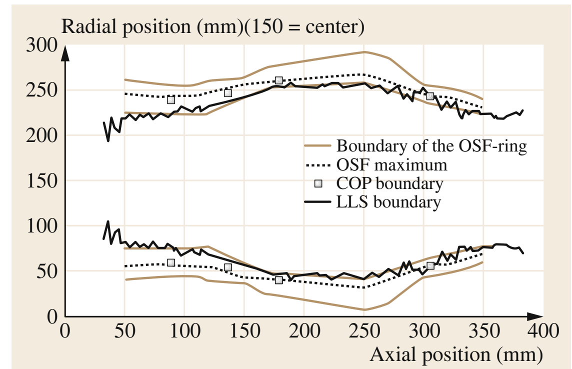

Fig. 5.27 Variations in the OSF ring width and its radial location in comparison to the variations of the COP and LLS boundaries along the crystal axis. The LLS defects were detected on the as-polished wafer surface, which detects only the larger voids, while the COP boundary was determined by LLS measurements after repeated SC1 cleaning, which enlarges the voids to above the LLS detection limit

adjacent to the former vacancy peaks coincide with pronounced minima in the interstitial oxygen content.

Considerable changes in the widths and the radial positions of OSF rings are observed if the crystals are nitrogen-doped. With increasing nitrogen content, the outer and inner OSF ring boundaries are shifted towards the crystal center [5.96]. However, the shift is much larger for the inner OSF ring boundary, resulting in a significant widening of the OSF ring width (Fig. 5.26) until it extends over the entire crystal volume. This behavior was tentatively explained by a schematic model that takes into account the slower build-up of vacancy supersaturation due to the formation of N_2V complexes and the resulting lower void nucleation temperature. The model also predicts that the void and the OSF region overlap, roughly in the area between the inner boundary and the middle of the OSF ring, which is in agreement with experimental data (Fig. 5.27).

In contrast to nitrogen, carbon tends to suppress OSF formation. This is again an indication that the mechanism of the effect of carbon is different. The above-mentioned idea of heterogeneous nucleation due to small carbon clusters may also explain this behavior. As heterogeneous nucleation needs less supersaturation, it prevails over homogeneous nucleation. Furthermore, the density of carbon clusters is much higher than that of homogeneously nucleated oxygen precipitates. Thus, the heterogeneously nucleated oxygen precipitates cannot grow to the critical size due to their large densities.

References

5.1 P.M. Petroff, A.J.R. de Kock: J. Cryst. Growth **30**, 117 (1975)
5.2 S. Sadamitsu, S. Umeno, Y. Koike, M. Hourai, S. Sumita, T. Shigematsu: Jpn. J. Appl. Phys. **32**, 3675 (1993)
5.3 L.I. Bernewitz, B.O. Kolbesen, K.R. Mayer, G.E. Schuh: Appl. Phys. Lett. **25**, 277 (1975)
5.4 B.O. Kolbesen, A. Mühlbauer: Solid State Electron. **25**, 759 (1982)
5.5 W. Bergholz, W. Mohr, W. Drewes: Mater. Sci. Eng. **B4**, 359 (1989)
5.6 M. Itsumi, H. Akiya, T. Ueki, M. Tomita, M. Yamawaki: J. Appl. Phys. **78**(10), 5984 (1995)
5.7 M. Miyazaki, S. Miyazaki, Y. Yanase, T. Ochiai, T. Shigematsu: Jpn. J. Appl. Phys. **34**, 6303 (1995)
5.8 J.G. Park, J.M. Park, K.C. Cho, G.S. Lee, H.K. Chung: Effect of crystal defects in device characteristics, Proc. 2nd Int. Symp. Adv. Sci. Technol. Silicon Materials, Kona-Hawaii, ed. by M. Umeno (1996) p. 2519
5.9 M. Itsumi: Mater. Sci. Eng. **B73**, 184 (2000)
5.10 T. Bearda, M. Houssa, P. Mertens, J. Vanhellemont, M. Heyns: Appl. Phys. Lett. **75**(9), 1255 (1999)
5.11 U. Lambert, A. Huber, J. Grabmeier, J. Vanhellemont, R. Wahlich, G. Kissinger: Microelectron. Eng. **48**, 127 (1999)
5.12 E. Dornberger, D. Temmler, W. v. Ammon: J. Electrochem. Soc. **149**(4), G226 (2002)
5.13 C. Kupfer, H. Roth, H. Dietrich: Mat. Sci. Semicon. Proc. **5**, 381 (2003)
5.14 A.M. Eidenzon, N.I. Puzanov: Inorg. Mater. **33**(3), 272 (1997)
5.15 J.G. Park, H.K. Chung: Wafer requirements: Memory devices, Proc. Silicon Wafer Symp., Portland (1999) p. D1
5.16 J.G. Park: J. Jpn. Assoc. Cryst. Growth **27**(2), 14 (2000)
5.17 R. Falster: Advances of the defect engineering of polished silicon wafers: Perfect silicon and magic denuded zones, Proc. Silicon Wafer Symp., Portland (1999) p. E13
5.18 D. Gräf, M. Suhren, U. Lambert, R. Schmolke, A. Ehlert, W. v. Ammon, P. Wagner: J. Electrochem. Soc. **145**(1), 275 (1998)
5.19 X. Yu, D. Yang, X. Ma, L. Li, D. Que: Semicond. Sci. Technol. **18**, 399 (2003)
5.20 K. Sumino, I. Yonenaga, M. Imai, T. Abe: J. Appl. Phys. **54**(9), 5016 (1983)
5.21 L. Jastrzebski, G.W. Cullen, R. Soydan, G. Harbeke, J. Lagowski, S. Vecrumba, W.N. Henry: J. Electrochem. Soc. **134**(2), 466 (1987)
5.22 G. Wang, D. Yang, D. Li, Q. Shui, J. Yang, D. Que: Physica B **308–310**, 450 (2001)
5.23 D. Maroudas, R. Brown: Appl. Phys. Lett. **62**(2), 172 (1993)
5.24 A. Seeger, K.P. Chik: Phys. Status Solidi A **29**, 455 (1968)
5.25 H.R. Schober: Phys. Rev. B **39**, 13013 (1989)
5.26 R. Car, P.J. Kelly, A. Oshiyama, S.T. Pantelides: Phys. Rev. Lett. **52**, 1814 (1984)
5.27 D. Maroudas, R. Brown: Phys. Rev. B **47**(23), 15562 (1993)
5.28 G.D. Watkins: Mater. Sci. Semicond. Process. **3**, 227 (2000)
5.29 N.A. Stolwijk, J. Holzl, W. Frank, E.R. Weber, H. Mehrer: Appl. Phys. A **39**, 37 (1986)
5.30 H. Bracht, N.A. Stolwijk, H. Mehrer: Phys. Rev. B **52**, 16542 (1995)
5.31 H. Zimmermann, H. Ryssel: Appl.Phys. A **55**, 121 (1992)
5.32 H. Bracht: Native point defects in silicon, Proc. 3rd Int. Symp. Defects Silicon III, Seattle, ed. by T. Abe, W.M. Bullis, S. Kobayashi, W. Lin, P. Wagner (1999) p. 357
5.33 W. v. Ammon, E. Dornberger, H. Oelkrug, H. Weidner: J. Cryst. Growth **151**, 273 (1995)
5.34 M. Hourai, E. Kajita, T. Nagashima, H. Fujiwara, S. Umeno, S. Sadamitsu, S. Miki, T. Shigematsu: Mater. Sci. Forum **196–201**, 1713 (1995)
5.35 E. Dornberger, W. v. Ammon: J. Electrochem. Soc **143**(5), 1648 (1996)

5.36 T. Sinno, R.A. Brown, W. v. Ammon, E. Dornberger: Appl. Phys. Lett. **70**(17), 2250 (1997)
5.37 M. Akatsuka, M. Okui, N. Morimoto, K. Sueoka: Jpn. J. Appl. Phys. **40**, 3055 (2001)
5.38 R. Falster, V.V. Voronkov, F. Quast: Phys. Status Solidi B **222**, 219 (2000)
5.39 N. Fukata, A. Kasuya, M. Suezawa: Jpn. J. Appl. Phys. **40**, L854 (2001)
5.40 D.A. Antoniadis, I. Moskowitz: J. Appl. Phys. **53**(10), 6780 (1982)
5.41 H.J. Gossmann, C.S. Rafferty, A.M. Vredenberg, H.S. Luftman, F.C. Unterwald, D.J. Eaglesham, D.C. Jacobson, T. Boone, J.M. Poate: Appl. Phys. Lett. **64**(3), 312 (1994)
5.42 T. Sinno: Thermophysical properties of intrinsic point defects in crystalline silicon, Proc. 9th Int. Symp. Silicon Mater. Sci. Technol. Semicond. Silicon, Philadelphia, ed. by H.R. Huff, L. Fabry, S. Kishino (The Electrochemical Society, Pennington 2002) p. 212
5.43 T. Frewen, T. Sinno, E. Dornberger, R. Hoelzl, W. v. Ammon, H. Bracht: J. Electrochem. Soc. **150**(11), G673 (2003)
5.44 K. Nakamura, R. Suewaka, B. Ko: ECS Solid State Lett. **3**(3), N5 (2014)
5.45 K. Sueoka, E. Kamiyama, J. Vanhellemont, K. Nakamura: ECS Solid State Lett. **3**(6), P69 (2014)
5.46 K. Sueoka, E. Kamiyama, J. Vanhellemont: J. Appl. Phys. **114**, 153510 (2013)
5.47 T. Ueki, M. Itsumi, T. Takeda: Jpn. J. Appl. Phys. **37**, 1669 (1998)
5.48 M. Itsumi: J. Cryst. Growth **237–239**, 1773 (2002)
5.49 S. Umeno, Y. Yanase, M. Hourai, M. Sano, Y. Shida, H. Tsuya: Jpn. J. Appl. Phys. **38**, 5725 (1999)
5.50 M. Nishimura, Y. Yamaguchi, K. Nakamura, J. Jablonski, M. Watanabe: Electrochem. Soc. Symp. Proc. **13**, 188 (1998)
5.51 J. Ryuta, E. Morita, T. Tanaka, Y. Shimanuki: Jpn. Appl. Phys. **29**, L1947 (1990)
5.52 H. Yamagishi, I. Fusegawa, N. Fujimaki, M. Katayama: Semicond. Sci. Techn. **7**, A135 (1992)
5.53 P.J. Roksnoer, M.M.B. Van de Boom: J. Cryst. Growth **53**, 563 (1981)
5.54 H. Bender, J. Vanhellemont, R. Schmolke: Jpn. J. Appl. Phys. **36**, L1217 (1997)
5.55 R. Schmolke, W. Angelberger, W. v. Ammon, H. Bender: Solid State Phenom. **82–84**, 231 (2002)
5.56 K. Nakai, M. Hasebe, K. Ohta, W. Ohashi: J. Cryst. Growth **210**, 20 (2000)
5.57 H. Föll, B.O. Kolbesen: Appl. Phys. **8**, 319 (1975)
5.58 P.M. Petroff, A.J.R. de Kock: J. Cryst. Growth **36**, 1822 (1976)
5.59 J. Chikawa, T. Abe, H. Harada: Impurity effect on the formation of microdefects during silicon crystal growth. In: *Semiconductor Silicon*, ed. by H.R. Huff, T. Abe, B. Kolbesen (The Electrochemical Society, Pennington 1986) p. 61
5.60 H. Föll, U. Gösele, B.O. Kolbesen: J. Cryst. Growth **40**, 90 (1977)
5.61 R. Schmolke, M. Blietz, R. Schauer, D. Zemke, H. Oelkrug, W.V. Ammon, U. Lambert, D. Gräf: In: *Advanced Silicon Wafers for 0.18 μmDesign Rule and Beyond: Epi and fLASH!*, *High Purity Silicon VI*, *Phoenix 2000*, ed. by C.L. Claeys, P. Rai-Choudhury, M. Watanabe, P. Stallhofer, H.J. Dawson (The Electrochemical Society, Pennington 2000)
5.62 W. v. Ammon, E. Dornberger, P.O. Hansson: J. Cryst. Growth **198/199**, 390 (1999)
5.63 V.V. Voronkov: J. Cryst. Growth **59**, 625 (1982)
5.64 E. Dornberger, J. Esfandyari, D. Gräf, J. Vanhellemont, U. Lambert, F. Dupret, W. v. Ammon: In: *Simulation of Grown-in Voids in Czochralski Silicon Crystals*, *Crystalline Defects and Contamination Control: Their Impact and Control in Device Manufacturing II*, *Nürnberg 1997*, ed. by B.O. Kolbesen, P. Stallhofer, C. Claeys, F. Tardiff (The Electrochemical Society, Pennington 1997)
5.65 M. Hasebe, Y. Takeoka, S. Shinoyama, S. Naito: Ring-like distributed stacking faults in CZ-Si wafers. In: *Defect Control in Semiconductors*, ed. by K. Sumino (Elsevier, Amsterdam 1990) p. 157
5.66 H. Yamagishi, I. Fusegawa, K. Takano, E. Iino, N. Fujimaki, T. Ohta, M. Sakurada: In: *Evaluation of FDPs and COPs in Silicon Single-Crystals*, *Semiconductor Silicon*, *San Francisco 1994*, ed. by H.R. Huff, W. Bergholz, K. Sumino (The Electrochemical Society, Pennington 1994)
5.67 W. v. Ammon, E. Dornberger: In: *Properties of Crystalline Silicon*, EMIS Datareviews, Vol. 20, ed. by R. Hull (INSPEC, London 1999)
5.68 V.V. Voronkov, R. Falster: J. Cryst. Growth **194**, 76 (1998)
5.69 E. Dornberger, D. Gräf, M. Suhren, U. Lambert, P. Wagner, F. Dupret, W. v. Ammon: J. Cryst. Growth **180**, 343 (1997)
5.70 E. Dornberger, J. Esfandyari, J. Vanhellemont, D. Gräf, U. Lambert, F. Dupret, W. v. Ammon: In: *Simulation of Non-Uniform Grown-in Void Distributions in Czochralski Crystal Growth*, *Semiconductor Silicon*, *San Francisco 1998*, ed. by H.R. Huff, U. Gösele, H. Tsuya (The Electrochemical Society, Pennington 1998)
5.71 M. Hourai, T. Nagashima, E. Kajita, S. Miki: In: *Oxygen Precipation Behavior in Silicon During Czochralski Crystal Growth*, *Semiconductor Silicon*, *San Francisco 1994*, ed. by H.R. Huff, W. Bergholz, K. Sumino (The Electrochemical Society, Pennington 1994) p. 156
5.72 T. Iwasaki, A. Tomiura, K. Nakai, H. Haga, K. Kojima, T. Nakashizu: In: *Influence of Cooling Condition During Crystal Growth of CZ-Si on Oxide Breakdown Property*, *Semiconductor Silicon*, *San Francisco 1994*, ed. by H.R. Huff, W. Bergholz, K. Sumino (The Electrochemical Society, Pennington 1994) p. 744
5.73 K. Takano, K. Kitagawa, E. Iino, M. Kimura, H. Yamagishi: Mater. Sci. Forum **196–201**, 1707 (1995)
5.74 M. Akatsuka, M. Okui, S. Umeno, K. Sueoka: J. Electrochem. Soc. **150**(9), G587 (2003)
5.75 J. Furukawa, H. Tanaka, Y. Nakada, N. Ono, H. Shiraki: J. Cryst. Growth **210**, 26 (2000)
5.76 V.V. Voronkov, R. Falster: J. Appl. Phys. **86**(11), 5975 (1999)

5.77 A. Natsume, N. Inoue, K. Tanahashi, A. Mori: J. Cryst. Growth **225**, 221 (2001)
5.78 T. Sinno, E. Dornberger, W. v. Ammon, R.A. Brown, F. Dupret: Mater. Sci. Eng. **28**, 149 (2000)
5.79 Z. Wang, R. Brown: J.Crystal Growth **231**, 442 (2001)
5.80 A. Sattler, W. von Ammon, M. Weber, W. Haeckl, H. Schmidt: Semiconductor Wafers of Silicon and Method for Their Production, US Patent Application 8 043 427B2 (2007)
5.81 K. Tanahashi, N. Inoue: J. Mat. Sci. Mater. Electron. **10**, 359 (1999)
5.82 J. Vanhellemont, E. Kamiyama, K. Sueoka: ECS Solid State Lett. **3**(5), X3–X4 (2014)
5.83 K. Sueoka, E. Kamiyama, J. Vanhellemont, K. Nakamura: Phys. Stat. sol. B **251**(11), 2159 (2014)
5.84 E. Dornberger, W. v. Ammon, D. Gräf, U. Lambert, A. Miller, H. Oelkrug, A. Ehlert: The impact of dwell time above 900 °C during crystal growth on the gate oxide integrity of silicon wafers, Proc. 4th Int. Symp. High Purity Silicon, San Antonio, ed. by C.L. Claeys, P. Rai-Choudhury, M. Watanabe, P. Stallhofer, H.J. Dawson (1996) p. 140
5.85 J. Esfandyari, G. Hobler, S. Senkader, H. Pötzl, B. Murphy: J. Electrochem. Soc. **143**, 995 (1996)
5.86 V.V. Voronkov, R. Falster: J. Cryst. Growth **198/199**, 399 (1999)
5.87 V.V. Voronkov, R. Falster: J. Appl. Phys. **87**(9), 4126 (2000)
5.88 T.A. Frewen, S.S. Kapur, W. Haeckl, W. v. Ammon, T. Sinno: J. Cryst. Growth **279**, 258 (2005)
5.89 N.I. Puzanov, A.M. Eidenzon: Semicond. Sci. Technol. **7**, 406 (1992)
5.90 K. Nakamura, T. Saishoji, J. Tomioka: J. Cryst. Growth **237–239**, 1678 (2002)
5.91 V.V. Voronkov: Mater. Sci. Eng. **B73**, 69 (2000)
5.92 V.V. Voronkov, R. Falster: J. Cryst. Growth **226**, 192 (2001)
5.93 T. Abe, M. Kimura: In: *Semiconductor Silicon, 1990*, ed. by H.R. Huff, K. Barraclough, J. Chikawa (The Electrochemical Society, Pennington 1990)
5.94 W. v. Ammon, P. Dreier: Silicon bulk technology for power devices, Proc. Int. Symp. Power Semicond. Devices, Tokyo (1988) p. 134
5.95 D.-R. Yang, Y.-W. Wang, H.-N. Yao, D.-L. Que: Prog. Nat. Sci. **3**(2), 176 (1993)
5.96 W. v. Ammon, R. Hoelzl, T. Wetzel, D. Zemke, G. Raming, M. Blietz: Microelectron. Eng. **66**, 234 (2003)
5.97 W.V. Ammon, A. Ehlert, U. Lambert, D. Gräf, M. Brohl, P. Wagner: In: *Gate Oxide Related Bulk Properties of Oxygen Doped Floating Zone and Czochralski Silicon*, *Semiconductor Silicon, San Francisco 1994*, ed. by H.R. Huff, W. Bergholz, K. Sumino (The Electrochemical Society, Pennington 1994)
5.98 K. Nakai, Y. Inoue, H. Yokota, A. Ikari, J. Takahashi, A. Tachikawa, K. Kitahara, Y. Ohta, W. Ohashi: J. Appl. Phys. **85**(8), 4301 (2001)
5.99 J. Takahashi, K. Nakai, K. Kawakami, Y. Inoue, H. Yokota, A. Tachikawa, A. Ikari, W. Ohashi: Jpn. J. Appl. Phys. **42**, 363 (2003)
5.100 F. Shimura, R.S. Hockett: Appl. Phys. Lett. **48**, 224 (1986)
5.101 Q. Sun, K.H. Yao, H.C. Gatos, J. Lagowski: J. Appl. Phys. **71**(8), 3760 (1992)
5.102 K. Aihara, H. Takeno, Y. Hayamizu, M. Tamatsuka, T. Masui: J. Appl. Phys. **88**(6), 3705 (2000)
5.103 K. Nakai, Y. Inoue, H. Yokota, A. Ikari, J. Takahashi, W. Ohashi: Formation of grown-in defects in nitrogen doped CZ-Si crystals, Proc 3rd Int. Symp. Adv. Sci. Technol. Silicon Materials, Kona, ed. by M. Umeno (2000) p. 88
5.104 D. Gräf, U. Lambert, R. Schmolke, R. Wahlich, W. Siebert, E. Daub, W. v. Ammon: 300 mm Epi pp-wafer: Is there sufficient gettering?, Proc. 6th Int. Symp. High Purity Silicon, Seattle, ed. by C.L. Claeys, P. Rai-Choudhury, M. Watanabe, P. Stallhofer, H.J. Dawson (2000) p. 319
5.105 H.J. Stein: Nitrogen in crystalline silicon, Proc. Int. Symp. Oxyg. Carbon, Hydrog. Nitrogen Cryst. Silicon, Boston, ed. by J.C. Mikkelsen Jr., S.J. Pearton, J.W. Corbett, S.J. Pennycook (1986) p. 523
5.106 Y. Itoh, T. Abe: Appl. Phys. Lett. **53**(1), 39 (1988)
5.107 A. Hara, A. Ohsawa: Interaction of oxygen and other point defects in silicon crystals, Proc. Int. Symp. Adv. Sci. Technol. Silicon Materials, Kona, ed. by K. Kohra (1991) p. 47
5.108 H. Sawada, K. Kawakami: Phys. Rev. B **62**(3), 1851 (2000)
5.109 H. Kageshima, A. Taguchi, K. Wada: Appl. Phys. Lett. **76**(25), 3718 (2000)
5.110 R. Jones, S. Öberg, F.B. Rasmussen, B.B. Nielson: Phys. Rev. Lett. **72**, 1882 (1994)
5.111 K.L. Brower: Phys. Rev. B **26**, 6040 (1982)
5.112 H.J. Stein: Appl. Phys. Lett. **47**(12), 1339 (1985)
5.113 K. Murakami, H. Itoh, K. Takita, K. Masuda: Appl. Phys. Lett. **45**(2), 176 (1984)
5.114 W.V. Ammon, D. Gräf, W. Zulehner, R. Schmolke, E. Dornberger, U. Lambert, J. Vanhellemont, W. Hensel: In: *Suppression of Point Defect Aggregation in FZ Silicon Single Crystals by Nitrogen Doping; Extendend Abstracts*, *Semiconductor Silicon, San Diego 1998*, ed. by H.R. Huff, U. Gösele, H. Tsuya (The Electrochemical Society, Pennington 1998)
5.115 K. Nakamura, T. Saishoji, S. Togawa, J. Tomioka: The effect of nitrogen on the grown-in defect formation in CZ silicon crystals. In: *Proceedings of the Kazusa Akademia Park Forum on the Science and Technology of Silicon Materials*, ed. by K. Sumino (Kazusa Akademia Park, Chiba 1999) p. 116
5.116 V.V. Voronkov, R. Falster: J. Electrochem. Soc. **149**(3), G167 (2002)
5.117 W.B. Knowlton, J.T. Walton, J.S. Lee, Y.K. Wong, E.E. Haller, W. v. Ammon, W. Zulehner: Mater. Sci. Forum **196–201**, 1761 (1995)
5.118 T. Ono, S. Umeno, T. Tanaka, E. Asayama, M. Hourai: Behavior of defects in nitrogen doped CZ-Si crystals, Proc. Int. Symp. Forum Sci. Technol. Silicon Materials, Shonan Village Center, Kanagawa, ed. by H. Yamata-Kaneta, K. Sumino (Japan Technical Information Service, Tokyo 2001) p. 95
5.119 K. Nakamura, T. Saishoji, S. Togawa, J. Tomioka: Influence of nitrogen on the pont defect reaction in

silicon, Proc. Int. Symp. Forum Sci. Technol. Silicon Materials, Shonan Village Cent., ed. by H. Yamata-Kaneta, K. Sumino (Japan Technical Information Service, Tokyo 2001) p. 109
5.120 W. v. Ammon, R. Hölzl, J. Virbulis, E. Dornberger, R. Schmolke, D. Gräf: J. Cryst. Growth **226**(1), 19 (2001)
5.121 P. Wagner, R. Oeder, W. Zulehner: Appl. Phys. A **46**, 73 (1988)
5.122 W. v. Ammon, P. Dreier, W. Hensel, U. Lambert, L. Köster: Mater. Sci. Eng. **B36**, 33 (1996)
5.123 M.W. Qi, S.S. Tan, B. Zhu, P.X. Cai, W.F. Gu, M. Xu, T.S. Shi, D.L. Que, L.B. Li: J. Appl. Phys. **69**, 3775 (1991)
5.124 A. Gali, J. Miro, P. Deak, C. Ewels, R. Jones: J. Phys. Condens. Mat. **8**, 7711 (1996)
5.125 X. Yue, J. Chen, X. Ma, D. Yang: Mater. Sci. Eng. **R74**, 1 (2013)
5.126 H.Ch. Alt, H.E. Wagner: J.Appl.Phys. **106**, 103511 (2009)
5.127 M. Suhren, D. Gräf, U. Lambert, P. Wagner: Crystal defects in highly boron doped silicon, Proc. 4th Int. Symp. High Purity Silicon, San Antonio, ed. by C.L. Claeys, P. Rai-Choudhury, M. Watanabe, P. Stallhofer, H.J. Dawson (The Electrochemical Society, Pennington 1996) p. 132
5.128 K. Nakamura, R. Suewaka, T. Saishoji, J. Tomioka: The effect of impurities on the grown-in defects in CZ-Si crystals (B, C, N, O, Sb, As, P), Proc. Forum Sci. Technol. Silicon Mater., ed. by H. Yamad-Kaneta, K. Sumino (2003) p. 161
5.129 W. v. Ammon: Crystal growth of large diameter CZ Si crystals, Proc 2nd Int. Symp. Adv. Sci. Technol. Silicon Materials, Kona, ed. by M. Umeno (1996) p. 233
5.130 J. Vanhellemont, E. Kamiyama, K. Sueoka: ECS J. Solid State Sci. Technol. **2**, 166 (2013)
5.131 T. Sinno, H. Susanto, R. Brown, W. v. Ammon, E. Dornberger: Appl. Phys. Lett. **75**, 1544 (1999)
5.132 S. Ma, S. Wang: Phys.Rev. B **81**, 193203 (2010)
5.133 T. Abe, T. Masui, H. Harada, J. Chikawa: In: *VLSI Science and Technology, 1985*, ed. by W.M. Bullis, S. Broyda (The Electrochemical Society, Pennington 1985)
5.134 R. Takeda, T. Minami, H. Saito, Y. Hirano, H. Fujimori, K. Kashima, Y. Matsushita: Influence of LSTD size on the formation of denuded zone in hydrogen-annealed CZ silicon wafers, Proc. 6th Int. Symp. High Purity Silicon, Phoenix, ed. by C.L. Claeys, P. Rai-Choudhury, M. Watanabe, P. Stallhofer, H.J. Dawson (The Electrochemical Society, Pennington 2000) p. 331
5.135 M. Porrini, V.V. Voronkov, R. Falster: Mater. Sci. Eng. B **134**, 185 (2006)
5.136 S. Kishino, M. Kanamori, N. Yoshihizo, M. Tajima, T. Iizuka: J. Appl. Phys. **50**, 8240 (1978)
5.137 T. Fukuda: Appl. Phys. Lett. **65**(11), 1376 (1994)
5.138 F. Shimura: J. Appl. Phys. **59**, 3251 (1986)
5.139 M. Porrini: Cryst. Res. Technol. **40**(10/11), 1054 (2005)
5.140 W. Sugimura, T. Ono, S. Umeno, M. Hourai, K. Sueoka: ECS Transactions **2**(2), 95 (2006)
5.141 V.V. Voronkov, R. Falster, M. Porrini, J. Duchini: Phys. Status Solidi A **209**(10), 1898 (2012)
5.142 M. Porrini, J. Duchini, A. Bazzali: Crystal. Res. Technol. **49**(8), 564 (2014)
5.143 T. Abe, H. Harada, J. Chikawa: Mat. Res. Soc. Symp. Proc. **14**, 1 (1983)
5.144 V.V. Voronkov, R. Falster: J. Electrochem. Soc. **149**, G167 (2002)
5.145 G. Borionetti, D. Gambaro, M. Porrini, V.V. Voronkov: Grown-in microdefect distribution in doped silicon crystals. In: *Semiconductor Silicon 2002–2*, ed. by H.R. Huff, L. Fabry, S. Kishino (Electrochemical Society, Pennington 2002) p. 505
5.146 K. Sueoka, M. Akatsuka, K. Nishihara, T. Yamamoto, S. Kobayashi: Mater. Sci. Forum **196–201**, 1737 (1995)
5.147 J. Vanhellemont, C. Claeys: J. Appl. Phys. **62**(9), 3960 (1987)